

# AHP-Net: adaptive-hyper-parameter deep learning based image reconstruction method for multilevel low-dose CT

Qiaoqiao Ding, Yuesong Nan, Hui Ji

*Department of Mathematics, National University of Singapore, Singapore 119076, SINGAPORE<sup>a)</sup>*

Hao Gao

*Department of Radiation Oncology, Winship Cancer Institute of Emory University, Atlanta, Georgia, 30322, USA<sup>b)</sup>*

**Purpose:** Low-dose CT (LDCT) imaging is desirable in many clinical applications to reduce X-ray radiation dose to patients. Inspired by deep learning (DL), a recent promising direction of model-based iterative reconstruction (MBIR) methods for LDCT is via optimization-unrolling DL-regularized image reconstruction, where pre-defined image prior is replaced by learnable data-adaptive prior. However, LDCT is clinically multilevel, since clinical scans have different noise levels that depend of scanning site, patient size, and clinical task. Therefore, this work aims to develop an adaptive-hyper-parameter DL-based image reconstruction method (AHP-Net) that can handle multilevel LDCT of different noise levels.

**Method:** AHP-Net unrolls a half-quadratic splitting scheme with learnable image prior built on framelet filter bank, and learns a network that automatically adjusts the hyper-parameters for various noise levels. Each stage of the AHP-Net contains one inversion block and a denoising block, where the denoising block is built-on a CNN. The main difference of the proposed AHP-Net from other deep learning solutions lies the design of the inversion block. In the proposed inversion block, we replaced the often-used gradient operator  $\nabla$  by the filter banks with 8 high-pass filters from linear spline framelet transform, motivated by its success in  $\ell_1$ -norm relating regularization in image recovery. Moreover, we proposed to pay special attention to the hyper-parameters involved in the inversion block, and presented a MLP-based NN to predict hyper-parameters that adaptive to both dose level and image content.

**Result:** AHP-Net provides a single universal training model that can handle multilevel LDCT. Extensive experimental evaluations using clinical scans suggest that AHP-Net outperformed conventional MBIR techniques and state-of-the-art deep-learning-based methods for multilevel LDCT of different noise levels.

**Conclusions:** The experiments showed the advantage of the proposed method over classic non-learning methods and some representative deep learning based methods for LDCT reconstruction. Also, another advantage is that the proposed method can only train a single model with competitive performance to process measurement data with varying dose levels.

**keywords:** X-ray CT, Image reconstruction, Low Dose CT, Deep Neural Networks

## I. INTRODUCTION

X-Ray Computed Tomography (CT) is to provide high-resolution three-dimensional (3D) images of internal anatomical structures using X-ray scanning and computational tomographic imaging techniques. As excessive exposure to radiation from X-ray CT scanner may increase the risk of damage to issue, many techniques have been developed to use less radiation than conventional CT scan, including decreasing the number of projection views<sup>42</sup> and lowering the X-ray tube current<sup>48</sup>. The latter is the so-called low-dose CT (LDCT). As a result, the signal-to-noise ratio (SNR) of the measurements collected from is much lower than that of conventional CT, which has a negative impact on the quality of the reconstructed image.

Given measurements from LDCT with low SNR, the images reconstructed by conventional filtered back-projection (FBP) method are often of poor quality with noticeable artifacts. In such a setting, the so-called model-based iterative

reconstruction (MBIR) method<sup>37,45</sup> is more widely used for image reconstruction. In MBIR, image reconstruction is usually formulated as an optimization problem regularized by certain functional for suppressing noise magnification during reconstruction. Such a regularization term is derived from some pre-defined prior on the image. In the past, many different priors have been proposed for MBIR-based reconstruction, e.g., total variation (TV)<sup>7,43,54</sup>, wavelet tight frame-based sparsity prior<sup>18,29</sup>, nonlocal sparsity prior<sup>30</sup>, and low-rank based patch prior<sup>5,6,17,19</sup>. The resulting optimization problems from these MBIR-based methods usually need to call some iterative scheme to find an approximate solution. Instead of using some pre-defined prior for regularization, there are also some works<sup>3,51</sup> that use dictionary learning or sparsifying transform learning to learn image prior for regularization in LDCT image reconstruction.

In recent years, there has been rapid progress on the development of deep learning methods for image reconstruction in LDCT. Most existing methods, *e.g.*,<sup>1,12,23,27</sup>, are based on the so-called optimization unrolling, which replaces the step involving the image prior by a learnable function built on a deep neural network (NN). The performance of these optimization-unrolling-based deep learning methods is very promising in LDCT image reconstruction.

However, LDCT is clinically multilevel, since clinical scans have different noise levels that depend of scanning site, patient size, and clinical task. The multilevel nature of LDCT implies that hyper-parameters have to be either manually tuned or automatically accounted for during the iterative scheme. It is known that in addition to the choice of image prior, the setting of these hyper-parameters also plays an important role in the reconstruction; see *e.g.* <sup>25,40,51</sup>. How to automate the selection of appropriate hyper-parameters is an important yet challenging task in MBIR. The optimal values of these hyper-parameters depends on many factors<sup>11,22,25,31,40,46</sup>, including

- SNR of measurement data,
- content of target image for reconstruction,
- global convergence property and fast convergence rate.

In the past, taking the factors listed above into consideration, there has been an enduring effort on developing automatic selection strategies of hyper-parameters for regularization methods, *e.g.* <sup>3,11,22,31,40,46</sup>.

There are also several hyper-parameters involved in existing optimization-unrolling-based deep learning methods, which are either manually tuned-up<sup>23,36</sup> or are treated as one part of network weights to be learned in the training<sup>1,27,44</sup>. As a result, the setting of these hyper-parameter is optimized only for one specific noise level of measurement data. When processing the data with different noise levels, they need to train different networks w.r.t. different noise levels. Such a practice can be inconvenient and sometimes difficult in practical usage when noise level of data is unknown.

Furthermore, as these hyper-parameters are fixed as constants for different measurements which can correspond to the images with different contents. Such a constant treatment on hyper-parameters in existing deep learning methods<sup>23,50</sup> certainly is not optimal. Motivated by the practical value of processing data with unknown noise level and the need for better image quality in LDCT imaging, this paper aims to develop an adaptive-hyper-parameter DL-based image reconstruction method (AHP-Net) that can handle multilevel LDCT of different noise levels.

In AHP-Net, image prior and hyper-parameter selection are collaboratively learned by two NNs. AHP-Net is based on the unrolling of the so-called half-quadratic splitting method<sup>20</sup>. The proposed NN is composed by  $K$  stages, which corresponds to  $K$  outer iterations in the optimization method. Each stage contains two blocks

- **Inversion block** reconstructs an image using both the measurement and the estimate from the previous stage, whose hyper-parameters are predicted by a multi-layer perception neural network (MLP).
- **De-noising block** removes the artifacts of the estimate passed from the inverse block by a convolutional neural network (CNN).

Same as many existing methods, the de-noising block is implemented using a CNN. Our main contribution is not on the design of the denoising block, but on the design of inversion block.

There are two main differences between the proposed inversion block and those existing ones. One is that the regularization term we proposed is based on a fine-grained high-pass filter bank motivated from wavelet tight frames<sup>15</sup>, which is different from gradient operator or learnable filter bank adopted in existing related works. The other is that the inner-loop hyper-parameters involved in the inversion block is predicted by a learnable NN such that those hyper-parameters will be adaptive to different dose levels and different inputs, while they are constants in existing related works. Such an adaptivity not only brings performance advantage in LDCT image reconstruction, but also allows one to train a single NN model to process the data with unknown dose level.

Due to space limitation, we only discuss most related methods for LDCT image reconstruction, *e.g.*, deep learning based methods. One type of deep learning methods uses deep NN as a technique for post-processing the images reconstructed from some existing method. By treating the artifacts as noise in the reconstructed image, these methods train an NN-based image denoiser to remove the artifacts from the image for better quality. The NN for image denoising is trained by using the pairs of the image reconstructed from LDCT and its counterpart from conventional

CT. Different NN architectures have been proposed for such a denoiser, *e.g.* CNN<sup>10</sup>, residual encoder CNN<sup>9</sup>, residual network<sup>24,35</sup>, U-net<sup>24,32</sup> and generative adversarial network (GAN)/Wasserstein-GAN<sup>49,52</sup>, multi-resolution deep convolutional framelets neural network<sup>53</sup>. Instead of directly denoising images, Kang *et al.*<sup>33,34</sup> proposed to denoise wavelet transform coefficients of the images using an NN-based denoiser. Overall, in such a post-processing approach, deep learning does not get involved in the reconstruction and data consistence is omitted.

In recent years, a more popular deep-learning-based approach is based on optimization unrolling, which introduces NNs in the iterations of the MBIR by replacing image-prior-based operations by the function modeled using learnable NN<sup>8</sup>. In other words, the pre-defined image prior is replaced by a learnable prior using NN. There are two ways to train the NN. One is pre-training the NNs and then plug it into the iterations of some MBIR; see *e.g.* pre-trained CNN and autoencoder-based NNs. The other is training the NNs together with the MBIR; see *e.g.* <sup>1,2,4,21,26,27,39,44</sup>.

In addition to the training scheme, another main difference among different optimization-unrolling-based deep learning methods lies in what numerical solver is chosen for unrolling. Based on the alternating direction method of multipliers (ADMM), the ADMM-net is proposed in<sup>44</sup> for image reconstruction in compressed-sensing-based Magnetic Resonance Imaging (MRI). For consistent CT image reconstruction, Gupta *et al.*<sup>23</sup> proposed to unroll the proximal gradient methods with CNN-based learnable prior. For LDCT image reconstruction, the ADMM is used in<sup>27</sup> and the primal-dual hybrid gradient (PDHG) method is used in<sup>1</sup> for unrolling with learnable image prior.

Similar to most iterative schemes of MBIR, in these optimization-unrolling-based deep learning methods, how to set appropriate hyper-parameters is very important to the quality of reconstructed images; see *e.g.* <sup>23,50</sup>. Different from conventional methods, there few systematic studies that address the problem of hyper-parameter setting in deep learning methods for image reconstruction.

In existing deep learning methods, the hyper-parameters are either manually tuned-up<sup>23,50</sup> or are treated as a part of learnable NN parameters<sup>1,27</sup>. Both treatments are sub-optimal. The former can only take a few trials on the hyper-parameters, since training the NN is a very time-consuming process. The later usually cannot find optimal values for hyper-parameters either, as these hyper-parameters are treated the same as millions of other NN weights in the optimization. In addition, for measurement with different dose levels, these deep learning methods need to train different models to fit a specific noise level for optimal performance. There will be a performance hit if only one model is trained for processing the data with different dose levels.

## I.B. Roadmap

This paper is organized as follows. Section II briefly introduces the problem and outlines the proposed method. Section III presents the details of the proposed methods which are split into several parts. Firstly, Section III.A describes the half-quadratic splitting method whose each iteration contains two blocks: inversion block and denoising block. Secondly, Section III.B describes the details of inversion block whose hyper-parameters are predicted by a learnable MLP. Thirdly, Section III.C describes the CNN-based implementation of the denoising block. Lastly, Section III.D summarizes the proposed methods. The implementation details of NN is given in Section IV. Section V is devoted to experimental evaluation and the comparison to other methods. Section VI concludes the paper.

## II. MEASUREMENT MODEL AND PROBLEM FORMULATION

In CT imaging with a mono-energetic source, the projection measurements from CT scan follow the Poisson distribution<sup>13,14</sup>, which can be expressed as:

$$\bar{y}_i \sim \text{Poisson}\{I_i \exp(-[\mathbf{A}\mathbf{x}]_i)\} + \mathcal{N}(0, \sigma_e^2), \quad (1)$$

where  $\mathcal{N}$  refers to normal distribution,  $\mathbf{x} = [x_j]_{j=1}^{N_p}$  denotes the attenuation map.  $\bar{\mathbf{y}} = [\bar{y}_i]_{i=1}^{N_d}$  represents the vector of measured projections.  $\mathbf{A} = [a_{i,j}]_{i,j}$  is the  $N_d \times N_p$  system matrix. The quantity  $[\mathbf{A}\mathbf{x}]_i = \sum_{j=1}^{N_p} a_{ij}x_j$  refers to the line integral of the attenuation map  $\mathbf{x}$  along the  $i$ -th X-ray.  $I_i$  represents the incident X-ray intensity incorporating X-ray source illumination and the detector efficiency. The quantity  $\sigma_e^2$  denotes the variance of the background electronic noise which is considered to be stable for a commercial CT scanner.

It is noted that the noise level varies for different target images. Given a target image  $\mathbf{x}$ , its noise level is controlled by  $I_i$ , *i.e.*, the measure data is corrupted with noise which becomes larger when dose level  $I_i$  decreases. However, even with a fixed dose level  $I_i$ , for different patients or different parts of human-body, their corresponding noise levels are different too.

To reconstruct the attenuation map  $\mathbf{x}$ , one can first run the correction and the logarithm transform on the noisy measurements  $\bar{\mathbf{y}}$  to generate the so-called sinogram  $\mathbf{y} = [y_i]_{i=1}^{N_d}$ , whose relation to  $\mathbf{A}\mathbf{x}$  is often expressed as:

$$\mathbf{y}_i = [\mathbf{A}\mathbf{x}]_i + \mathcal{N}(0, \sigma_i^2), \quad (2)$$

where  $\sigma_i$  denotes the noise variance. The linear system (2) is ill-posed, and certain regularization needs to be imposed on the solution to resolve the solution ambiguity and suppress noise magnification. Let  $p(\mathbf{x}; \lambda)$  denotes the prior distribution function of  $\mathbf{x}$  with distribution parameter  $\lambda$ . The maximum a posterior (MAP) estimation of  $\mathbf{x}$  is then the minimum of the cost function given by

$$\min_{\mathbf{x}} \frac{1}{2} \|\text{diag}(\sigma_i^{-1})(\mathbf{A}\mathbf{x} - \mathbf{y})\|_2^2 + \log p(\mathbf{x}; \lambda), \quad (3)$$

where the first is data fidelity term and the second is regularization term on  $\mathbf{x}$  derived from its prior distribution. The model (3) is often called penalized weighted least-squares (PWLS) image reconstruction model<sup>16,41,45</sup>, a widely used one in CT image reconstruction.

Many regularization terms  $\log p(\mathbf{x}; \lambda)$  have been proposed for LDCT image reconstruction, *e.g.* TV<sup>43</sup>, nonlocal TV<sup>30</sup> and framelet<sup>29</sup>. These regularization functionals are usually not directly defined in image domain, but in the domain of image gradients or their generalizations. For example, both the TV and wavelet-transform-based regularizations take the form of  $\lambda \|\Gamma \mathbf{x}\|_1$ , where  $\Gamma$  is the gradient operator  $\nabla$  (TV) or wavelet transform  $W$  (wavelet). The prior distribution parameter  $\lambda$  is also called the regularization parameter, which needs to be set in advance.

There are many numerical scheme for solving (3) with  $p(\mathbf{x}; \lambda) = \lambda \|\Gamma \mathbf{x}\|_1$ , *e.g.* ADMM and PDHG. In this paper, our work is based on the half-quadratic splitting method<sup>20</sup>, which solve the problem (3) by introducing an auxiliary variable  $\mathbf{z}$ . Suppose  $\text{diag}(\sigma_i) = \sigma \mathbf{I}$ ,

$$\textbf{Inversion} : \mathbf{x}^k = \arg \min_{\mathbf{x}} \frac{1}{\sigma^2} \|\mathbf{A}\mathbf{x} - \mathbf{y}\|_2^2 + \frac{1}{\mu^k} \|\Gamma \mathbf{x} - \mathbf{z}^k\|_2^2, \quad (4a)$$

$$\textbf{Denoising} : \mathbf{z}^{k+1} = \arg \min_{\mathbf{z}} \lambda \|\mathbf{z}\|_1 + \frac{1}{\mu^k} \|\Gamma \mathbf{x}^k - \mathbf{z}\|_2^2, \quad (4b)$$

where  $\{\mu_k\}_k$  is the parameter sequences of the algorithm. The noise variance  $\sigma$ , the hyper-parameters, including the parameter sequence  $\{\mu_k\}_k$ , and the regularization parameter  $\lambda$ , will make a noticeable impact on the convergence behavior and the quality of the result.

There are two blocks in the iterative scheme (4). The first is an inversion block (4a), which reconstructs an image from the measurement  $\mathbf{y}$  and the estimate from the previous iteration. The second is a denoising block (4b), which refines the estimate from the inverse block using the prior-based regularization. The performance of the scheme (4) depends on the answers to the following two questions.

1. what prior  $p(\mathbf{x}; \lambda)$  fits the target image  $\mathbf{x}$  well?
2. what values of the hyper-parameters are optimal for estimating  $\mathbf{x}$ ?

Most existing optimization-unrolling methods focus on the replacement of the denoising block (4b) using a NN-based denoiser. Despite the importance of the hyper-parameters<sup>23</sup>, the current treatment on the setting of hyper-parameters is done by either manual selection or learning them as one part of NN weights.

This paper aims at designing a deep learning method for LDCT reconstruction that not only uses a CNN-based denoiser to replace (4b), but also introduce a MAP-based predictor in the inversion block (4a) to automate the adaptive setting of hyper-parameters to the SNR of measurement data and the target image  $\mathbf{x}$ . The proposed deep learning method not only provides very competitive performance for LDCT image reconstruction, but also is universal such that a single trained NN model can be used for the reconstruction of CT measurements with varying dose levels.

### III. METHOD

In this section, we give a detailed discussion on the proposed deep learning method for LDCT reconstruction.

#### III.A. Detailed algorithm of the iterative scheme (4)

Recall that each iteration of the scheme (4) has two blocks: inversion block and denoising block. For the inversion block, the problem has an analytical solution given by

$$\mathbf{x}^k = \frac{1}{2} (\mathbf{A}^\top \mathbf{A} + \frac{\sigma^2}{\mu^k} \Gamma^\top \Gamma)^{-1} (\mathbf{A}^\top \mathbf{y} + \frac{\sigma^2}{\mu^k} \Gamma^\top \mathbf{z}^k).$$

In conventional methods such as TV method, the operator  $\Gamma$  is image gradient operator  $\nabla$  that convolves the image  $\mathbf{x}$  by two filters:  $[1, -1]$  and  $[1, -1]^\top$ . Motivated by the performance improvement of framelet transform over  $\nabla$  in many image recovery tasks, we propose to use the filter bank of spline framelet transform<sup>15</sup>. In our implementation, the filter bank of linear B-spline framelet transform is adopted, which contains totally 8 2D high-pass filters

$$\{\mathbf{f}_i\}_{i=1}^8 := \{h_{k_1} h_{k_2}^\top\}_{0 \leq k_1, k_2 \leq 2} \setminus \{h_0 h_0^\top\}, \quad (5)$$

composed by the tensor product of three 1D filters:

$$h_0 = [\frac{1}{4}, \frac{1}{2}, \frac{1}{4}]^\top, h_1 = [-\frac{1}{4}, \frac{1}{2}, \frac{1}{4}]^\top, h_2 = [\frac{\sqrt{2}}{4}, 0, -\frac{\sqrt{2}}{4}]^\top. \quad (6)$$

It can be seen that such a filter bank is composed of more fine-grained 2D filters on image gradients with different difference orders and along different directions. Then, the iterative scheme (4) can be re-formulated as

$$\mathbf{x}^k = \arg \min_{\mathbf{x}} \|\mathbf{A}\mathbf{x} - \mathbf{y}\|_2^2 + \sum_{i=1}^L \beta_i^k \|\mathbf{f}_i \otimes \mathbf{x} - \mathbf{z}_i^k\|_2^2, \quad (7)$$

$$\mathbf{z}_i^{k+1} = \arg \min_{\mathbf{z}_i} \|\mathbf{f}_i \otimes \mathbf{x}^k - \mathbf{z}_i\|_2^2 + \alpha_i^k \|\mathbf{z}_i\|_1, \quad 1 \leq i \leq L, \quad (8)$$

where  $\beta_i^k = \frac{\sigma^2}{\mu_i^k}$ ,  $\alpha_i^k = \frac{1}{\lambda_i \mu_i^k}$ . Again, the inversion block (7) has an analytical solution expressed by

$$\mathbf{x}^k = \left( \mathbf{A}^\top \mathbf{A} + \sum_{i=1}^L \beta_i^k \mathbf{F}_i^\top \mathbf{F}_i \right)^{-1} \left( \mathbf{A}^\top \mathbf{y} + \sum_{i=1}^L \beta_i^k \mathbf{F}_i^\top \mathbf{z}_i^k \right), \quad (9)$$

where  $\mathbf{F}_i$  denote the matrix form of the convolution operator with the filter  $\mathbf{f}_i$ .

In short, The inversion block (7) reconstructs  $\mathbf{x}$  from measurement data  $\mathbf{y}$  and the estimate of  $\mathbf{x}$  in high-pass channels using the least squares estimator, and the denoising block (8) refines the estimate of  $\{\mathbf{z}_i\}_i$  in high-frequency channels by treating the artifacts as noise and suppressing it via some regularization.

### III.B. Inversion block with an MLP-based adaptive predictor for hyper-parameters

Recall that in the analytical solution of the inversion block (9), there is a sequence of hyper-parameters  $\{\beta_i^k\}_{i=1}^L$ . The setting of such a sequence makes significant impact on the intermediate output, which in turn will make noticeable impact on the quality of the final result. In this section, we present a NN-based solution to predict  $\{\beta_i^k\}_{i=1}^L$  for optimal performance.

Indeed, the step (7) can be interpreted as an MAP estimator under the assumption that both  $\mathbf{y}$  and  $\mathbf{z}_i^k$  are the measurements of  $\mathbf{A}\mathbf{x}$  and  $\mathbf{F}_i\mathbf{x}$  corrupted by additive Gaussian white noise:

$$\mathbf{y} - \mathbf{A}\mathbf{x} = \mathbf{n} \sim \mathcal{N}(0, \sigma^2), \quad (10a)$$

$$\mathbf{z}_i^k - \mathbf{F}_i\mathbf{x} = \boldsymbol{\epsilon}_i^k \sim \mathcal{N}(0, (\sigma_i^k)^2), \quad 1 \leq i \leq L. \quad (10b)$$

In such a simplified case, one can have an explicit solution to the hyper-parameters:  $\beta_i^k := (\sigma_i^k)^{-2} \sigma^2$ .

Under the assumption (10), The two quantities  $\sigma_i$  and  $\sigma$  are encoded in the residual:

$$\mathbf{d}_i^k = \mathbf{F}_i\mathbf{y} - \mathbf{A}\mathbf{z}_i^k = -\mathbf{A}\boldsymbol{\epsilon}_i + \mathbf{F}_i\mathbf{n}.$$

It can be seen that the quality

$$\frac{1}{N_p} \|\mathbf{d}_i^k\|_2^2 = \sigma^2 \sum_{j=1}^{N_p} \frac{|\lambda_A[j]|^2}{N_p} \tilde{\mathbf{n}}[j]^2 + (\sigma_i^k)^2 \sum_{j=1}^{N_p} \frac{|\lambda_{F_i}[j]|^2}{N_p} \tilde{\boldsymbol{\epsilon}}_i[j]^2 \quad (11)$$

where  $\lambda_A, \lambda_{F_i}$  are the spectrum of  $\mathbf{A}, \mathbf{F}_i$ . The two vectors  $\{\tilde{\mathbf{n}}[j]^2\}_j, \{\tilde{\boldsymbol{\epsilon}}_i[j]^2\}_j$  are independent random variables following the same Chi-squared distribution:

$$\tilde{\mathbf{n}}[j]^2 \sim \chi(1); \quad \tilde{\boldsymbol{\epsilon}}_i[j]^2 \sim \chi(1), \quad 1 \leq j \leq N_p.$$

It can be seen from (11) that there exist some linear relationship between the quantity  $\frac{1}{N_p} \|\mathbf{d}_i^k\|_2^2$  and  $\sigma^2, (\sigma_i^k)^2$ . In practice, as the noise  $\mathbf{n}_i$  (i.e. the artifacts) is far more complex than additive Gaussian white noise. We thus propose to learn a non-linear function to model such relationship, i.e we automate the estimation of the hyper-parameter sequence  $\{\beta_i^k\}$  using a learnable NN. The NN, denoted by  $\mathcal{P}_{\text{mlp}}^k(\cdot; \theta_{\mathcal{P}}^k)$  with parameters  $\theta_{\mathcal{P}}^k$ , takes  $\{\|\mathbf{f}_i \otimes \mathbf{y} - \mathbf{A}\mathbf{z}_i^k\|_2^2\}_{i=1}^L$  as the input and outputs the estimation of  $\{\beta_i^k\}$ :

$$\mathcal{P}_{\text{mlp}}^k(\cdot, \theta_{\mathcal{P}}^k) : [\|\mathbf{d}_i^k\|_2^2]_{i=1}^L \in \mathbb{R}^L \rightarrow [\beta_i^k]_{i=1}^L \in \mathbb{R}^L. \quad (12)$$

An MLP is implemented for modeling the mapping  $\mathcal{P}^k$ , which contains 3 layers. Each layer is composed by one fully connected layer followed by one ReLU function. See Fig. 1 for the diagram of the proposed hyper-parameter predictor  $\mathcal{P}^k$ .

Once the sequence  $\{\beta_i^k\}_{i=1}^L$  is predicted, we can update the estimate using the analytical solution (9). As the matrix  $\mathbf{A}^\top \mathbf{A} + \sum_{i=1}^L \beta_i^k \mathbf{F}_i^\top \mathbf{F}_i$  is of large size in CT reconstruction, the gradient descent method is called to find an approximate solution. Note that the gradient of (7) is

$$\mathbf{g}^k(\mathbf{x}) = \mathbf{A}^\top (\mathbf{A}\mathbf{x} - \mathbf{y}) + \sum_{i=1}^L \beta_i^k \mathbf{F}_i^\top (\mathbf{F}_i\mathbf{x} - \mathbf{z}_i^k). \quad (13)$$

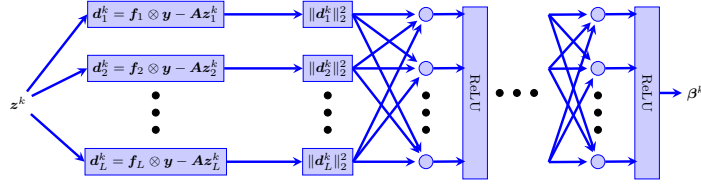


FIG. 1: Diagram of the MLP for predicting hyper-parameter sequence  $\beta^k = \{\beta_i^k\}_{i=1}^L$ , where  $\mathbf{z}^k = \{\mathbf{z}_i^k\}_{i=1}^L$ .

Then, we find an approximate solution to (7) using the gradient descent method:

$$\mathbf{x}_t^k = \mathbf{x}_{t-1}^k - \theta_{t-1}^k g^k(\mathbf{x}_{t-1}^k), \quad (14)$$

where  $t = 1, 2, \dots, T$ ,  $\mathbf{x}_0^k = \tilde{\mathbf{x}}^{k-1}$ ,  $\mathbf{x}^k = \mathbf{x}_T^k$ , and the vector  $\theta_{\mathcal{I}}^k = [\theta_0^k, \dots, \theta_{T-1}^k]$  is the vector of learnable step size. We denote such an approximate solution by

$$\mathcal{I}_{\text{gd}}^k(\cdot, \theta_{\mathcal{I}}^k) : [\mathbf{y}, \{\beta_i^k\}_{i=1}^L, \{\mathbf{z}_i^k\}_{i=1}^L] \rightarrow \mathbf{x}^k. \quad (15)$$

In summary, the inversion block can be expressed as

$$\mathcal{L}^k(\cdot; \{\theta_{\mathcal{P}}^k, \theta_{\mathcal{I}}^k\}) : [\mathbf{y}, \{\mathbf{z}_i^k\}_{i=1}^L] \rightarrow \mathbf{x}^k, \quad (16)$$

where  $\{\theta_{\mathcal{P}}^k, \theta_{\mathcal{I}}^k\}$  is the set of learnable weights, including the weights of the MLP and the step sizes of the gradient descent method.

### III.C. Denoising block with CNN-based adaptive prior

For the denoising block, following many existing methods, we also adopt a CNN to learn the function (8) such that the estimate passed from the inversion block can be refined using learnable prior that is adaptive to the target image. It is noted that the measurements of an image in different high-pass channels are high correlated. Independently running denoising in these high-pass channels is not a good practice as the inherent correlation is lost in such a process. Thus, the proposed CNN take the estimate  $\mathbf{x}^k$  as the input and output a denoised version  $\tilde{\mathbf{x}}^k$ , which is then fed to  $L$  ( $=8$  in our implementation) high-pass channels to have an estimate  $\mathbf{z}_i^{k+1}$ :

$$\mathbf{z}_i^{k+1} = \{\mathbf{f}_i \otimes \tilde{\mathbf{x}}^k\}_i, \quad 1 \leq i \leq L. \quad (17)$$

Such a procedure reserves the correlations of an image among different high-pass channels.

Furthermore, instead of only taking the previous estimate  $\mathbf{x}^k$  as the input, The CNN for denoising block takes all previous estimates  $\{\mathbf{x}^0, \mathbf{x}^1, \dots, \mathbf{x}^k\}$  as the input, which can alleviate the so-called vanishing gradient in training<sup>28</sup>. Another benefit of doing so is that the fusion of these previous estimates provide more information for the refinement, as these are different estimates of the truth with different types of artifacts. The final version of the mapping of the CNN-based denoising process can be expressed as

$$\mathcal{D}_{\text{cnn}}^k(\cdot, \theta_{\mathcal{D}}^k) : [\mathbf{x}^0, \mathbf{x}^1, \dots, \mathbf{x}^k] \rightarrow \tilde{\mathbf{x}}^k, \quad (18)$$

where  $\theta_{\mathcal{D}}^k$  denotes the parameters of denoising NN,  $\mathcal{D}_{\text{cnn}}^k$ . The output of the whole denoising block is then

$$\mathbf{z}_i^{k+1} = \mathbf{f}_i \otimes \mathcal{D}_{\text{cnn}}^k([\mathbf{x}^0, \mathbf{x}^1, \dots, \mathbf{x}^k], \theta_{\mathcal{D}}^k). \quad (19)$$

For each stage of the iteration, we use 17-block standard CNN with the structure Conv $\rightarrow$ BN $\rightarrow$ ReLU, except the first block and the last block. The BN layer is omitted for the first and last block. For all the Conv layers in the CNN, the kernel size is set as  $3 \times 3$ . The channel size is set to 64. See Fig. 2 for the diagram of the CNN-based denoising block. In summary, the denoising block can be expressed as

$$\mathcal{D}^k(\cdot; \theta_{\mathcal{D}}^k) : [\mathbf{x}^0, \mathbf{x}^1, \dots, \mathbf{x}^k] \rightarrow \mathbf{z}^{k+1}, \quad (20)$$

where  $\theta_{\mathcal{D}}^k$  is the set of learnable weights w.r.t. the CNN-based denoiser.

### III.D. The overall architecture of the proposed method

The proposed deep learning method for LDCT contains totally  $K + 1$  stages, denoted by  $\{\mathcal{S}^k\}_{k=0}^K$ . Let  $\mathcal{L}^k$  and  $\mathcal{D}^k$  denote the inversion block and denoising block defined by (16) and (20). Then, each stage corresponds to one iteration in MBIR as follows.

$$\mathcal{S}^0(\cdot; \Theta^0) : \quad \mathbf{y} \xrightarrow{\mathcal{L}^0} \mathbf{x}^0, \quad (21)$$

$$\mathcal{S}^k(\cdot; \Theta^k) : \quad [\mathbf{y}, \{\mathbf{x}^\ell\}_{\ell=0}^{k-1}] \xrightarrow{\mathcal{D}^{k-1}} [\mathbf{y}, \mathbf{z}^{k-1}] \xrightarrow{\mathcal{L}^k} \mathbf{x}^k, \quad (22)$$



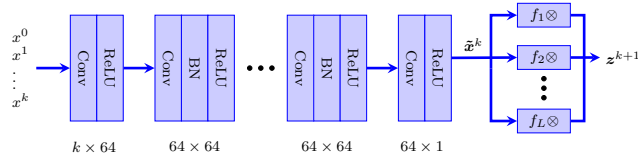


FIG. 2: Diagram of the CNN for denoising.

for  $k = 1, 2, \dots, K$ , where  $\Theta^k := \{\theta_D^{k-1}, \theta_P^k, \theta_I^k\}$  denotes the weights at the  $k$ -th stage, including the weights of  $\mathcal{D}_{\text{cnn}}^{k-1}$ ,  $\mathcal{P}_{\text{mlp}}^k$ , and step sizes of  $\mathcal{I}_{\text{gd}}^k$ . In stage  $S^0$ , we initialize  $\mathbf{z}^0 = \mathbf{0}$  and  $\beta_i^0 = 0.005$  for  $1 \leq i \leq L$ . It can be seen that when the measurement is fed to the proposed NN, it generates a sequence through the  $K + 1$  stages:

$$\{\mathbf{x}^0, \mathbf{x}^1, \dots, \mathbf{x}^K\},$$

The final output of the whole NN is defined as  $\mathbf{x}^* := \mathbf{x}^K$ . See Fig. 3 for the outline of the proposed NN for LDCT reconstruction, and we call it AHP-Net.

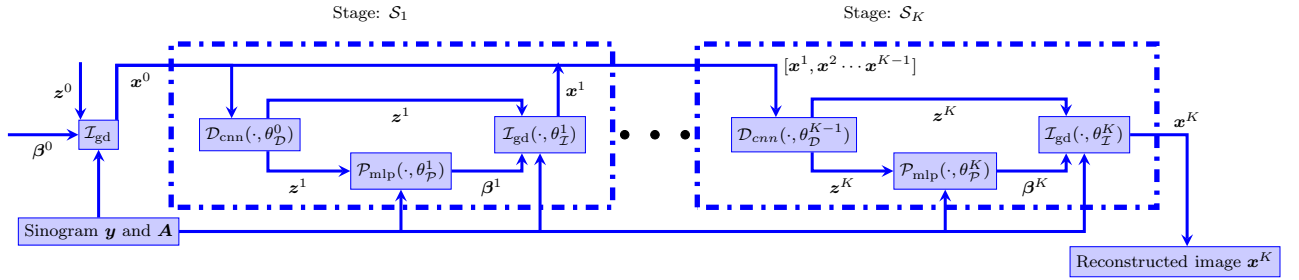


FIG. 3: Diagram of the proposed AHP-Net for LDCT image reconstruction.

For the training of the proposed AHP-Net, we consider the training dataset  $\{\mathbf{x}_j, \mathbf{y}_j\}_{j=1}^J$  with  $J$  training samples, where each  $(\mathbf{x}_j, \mathbf{y}_j)$  denotes one pair of normal dose image and low dose sinogram data. The loss function is defined as

$$\mathcal{L}(\Theta) = \frac{1}{J} \sum_{j=1}^J \left( \|\mathbf{x}_j^K - \mathbf{x}_j\|_2^2 + \sum_{k=1}^{K-1} \mu_k \|\mathbf{x}_j^k - \mathbf{x}_j\|_2^2 \right), \quad (23)$$

where  $\Theta := \{\Theta^k\}_{k=0}^K$  is the whole set of NN parameters, and

$$\mathbf{x}_j^k = (\mathcal{S}^k(\cdot; \Theta^k) \circ \mathcal{S}^{k-1}(\cdot; \Theta^{k-1}) \circ \dots \circ \mathcal{S}^0(\cdot; \Theta^0))(\mathbf{y}_j)$$

denotes the output of the AHP-Net at the  $k$ -th stage w.r.t. the input  $\mathbf{y}_j$ . The first term in (23) is for encouraging the output of the NN close to the truth. The second term is for ensuring the intermediate results not too far from the truth. The balancing parameters  $\{\mu_k\}_{k=1}^{K-1}$  are set to  $\frac{4}{5}$  throughout all experiments.

The weights of NN are then learned by minimizing the loss function (23) using the standard mini-batch stochastic gradient descent (SGD) method. The gradient of  $\Theta^K$  can be calculated via back-propagation. See supplementary materials for the detailed derivation of the calculation of the gradient. Once we finished the training of the model with an estimation of NN parameters  $\bar{\Theta}$ . For a low dose input data  $\mathbf{y}$ , the image can be reconstructed by fed it into the NN with parameters  $\bar{\Theta}$ :

$$\mathbf{x}^* := (\mathcal{S}^k(\cdot; \bar{\Theta}^k) \circ \mathcal{S}^{k-1}(\cdot; \bar{\Theta}^{k-1}) \circ \dots \circ \mathcal{S}^0(\cdot; \bar{\Theta}^0))(\mathbf{y}).$$

### III.E. Implementation

The proposed AHP-Net is implemented with  $K = 3$  stages. For the inversion block in each stage, the iteration number  $T$  is set to 3. For the proposed NN method, training is performed with PyTorch<sup>38</sup> interface on a NVIDIA Titan GPU. Adam method was used with the momentum parameter  $\beta = 0.9$ , mini-batch size to be 4, and the learning rate to be  $10^{-4}$ . The model was trained for 50 epochs. The convolution weight of  $\mathcal{D}_{\text{cnn}}$  for denoising were initialized with orthogonal matrices and the biases were initialized with zeros. All weights in  $\mathcal{P}_{\text{mlp}}$  were initialized to 1 and the biases to 0.

## IV. EXPERIMENTS

In this section, we conduct a comprehensive experimental evaluation of the proposed AHP-Net, and compare it to other representative methods in LDCT image reconstruction.

### IV.A. Dataset for evaluation

To evaluate the performance of the proposed method under different dose levels, we simulated low dose projection data from their normal-dose counterparts. The normal dose dataset included 6400 normal-dose prostate CT images of  $256 \times 256$  pixels per image from 100 anonymized scans, where 80% and 20% of the data is set for training and testing respectively. The LDCT projection data was simulated by adding Poisson noise onto the normal-dose projection data as Section II. The simulated geometry for projection data includes fan-beam CT scanner, flat-panel detector of  $0.388 \text{ mm} \times 0.388 \text{ mm}$  pixel size, 600 projection views evenly spanning a  $360^\circ$  circular orbit, 512 detector bins for each projection with 1 mm pixel size, 100.0 cm source to detector distance and 50.0 cm source to isocenter distance.

For the training dataset, 80 patients' simulated low-dose projection and corresponding normal dose images were selected as the pairs of measurement and truth image. For every patient's normal dose data, we simulated the low-dose measurement with uniform dose level. Then, the sinogram different patients was obtained by take logarithm on projection data  $\tilde{\mathbf{y}}$ . The remaining 20 scans were selected as testing dataset. For testing dataset, low dose measurement is simulated by the same way as training dataset. Throughout all experiments, 5120 pairs are included in training dataset, 1280 pairs in testing dataset.

### IV.B. Training scheme

Two types of training schemes are conducted in this paper.

- *Different models for different dose levels.* In this training scheme, for each dose level, all deep learning methods train one specific model using the measurements with the same dose level, and also test it on the measurements with the same dose level. Totally 4 dose levels are evaluated:  $I_i = 10^5, 5 \times 10^4, 10^4, 5 \times 10^3$ .
- *One universal model for different dose levels.* In this training scheme, all deep learning methods train a single model using the measurements with varying dose levels, and also test it on the measurements with varying dose levels. In this case, each measurement in training dataset is generated with its dose level randomly selected from  $\{10^5, 7.5 \times 10^4, 5 \times 10^4, 2.5 \times 10^4, 10^4, 7.5 \times 10^3, 5 \times 10^3\}$ , and each measurement in validation/testing dataset is generated by with its dose level  $I_i = 10^5, 5 \times 10^4, 10^4, 5 \times 10^3$  respectively.

### IV.C. Comparison Method

The performance of the proposed methods is evaluated in comparison with classic FBP method, TV method, FBPCnnNet, MoDL, and Neumann Network.

- The TV method was implemented using the ADMM solver:

$$\begin{aligned} \mathbf{x}^{k+1} &= \arg \min_{\mathbf{x}} \frac{1}{2} \|\mathbf{Ax} - \mathbf{y}\|_2^2 + \frac{\mu}{2} \|\nabla \mathbf{x} - \mathbf{z}^k + \frac{\mathbf{p}^k}{\mu}\|_2^2, \\ \mathbf{z}^{k+1} &= \arg \min_{\mathbf{z}} \lambda \|\mathbf{z}\|_1 + \frac{\mu}{2} \|\mathbf{z} - (\nabla \mathbf{x}^{k+1} + \frac{\mathbf{p}^k}{\mu})\|_2^2, \\ \mathbf{p}^{k+1} &= \mathbf{p}^k + \mu(\nabla \mathbf{x}^{k+1} - \mathbf{z}^{k+1}), \end{aligned}$$

The parameters  $\lambda, \mu$  of the TV method are manually tuned-up for optimal performance under different dose level. Specifically, the regularization parameter  $\lambda$  is set to 0.01 for  $I_i = 10^5, 5 \times 10^4$ ; 0.02 for  $I_i = 10^4$ ; and 0.03 for  $I_i = 5000$  and parameter  $\mu$  is set to 10.

- FBPCnnNet<sup>32</sup> is one representative method for CT reconstruction among all deep learning methods that use the deep NN as a post-process technique. In FBPCnnNet, a residual CNN with U-net architecture, is trained to directly denoise the image reconstructed by the FBP method.
- MoDL<sup>2</sup> is a deep learning method proposed for MRI reconstruction, which also can be used for LDCT reconstruction. MoDL unrolls the following iterative scheme

$$\begin{aligned} \mathbf{x}^k &= (\mathbf{A}^T \mathbf{A} + \lambda \mathbf{I})^{-1} (\mathbf{A}^T \mathbf{y} + \lambda \tilde{\mathbf{x}}^{k-1}), \\ \tilde{\mathbf{x}}^k &= \mathcal{D}_{\text{cnn}}(\mathbf{x}^k; \theta^k) \end{aligned}$$

where  $\mathcal{D}_{\text{cnn}}$  is a CNN-based denoiser and  $\lambda$  is learned as an NN weight.



TABLE I: Quantitative comparison (Mean $\pm$ STD) of the results reconstructed by different methods on testing dataset, where different models are trained for different dose levels in deep learning methods.

Dose level	Index	FBP	TV	FBPConvNet	MoDL	Neumann-Net	Our AHP-Net
$10^5$	PSNR	$37.15 \pm 2.04$	$39.75 \pm 2.18$	$41.17 \pm 2.11$	$35.17 \pm 2.14$	$32.51 \pm 2.57$	$41.12 \pm 2.69$
	RMSE	$19.06 \pm 1.10$	$14.18 \pm 1.38$	$12.04 \pm 1.27$	$24.20 \pm 3.87$	$33.70 \pm 11.47$	$12.41 \pm 3.31$
	SSIM	$0.9336 \pm 0.01$	$0.9685 \pm 0.01$	$0.9667 \pm 0.01$	$0.9442 \pm 0.02$	$0.8974 \pm 0.03$	$0.9739 \pm 0.01$
$5 \times 10^4$	PSNR	$35.78 \pm 2.05$	$38.85 \pm 2.18$	$39.66 \pm 2.14$	$34.81 \pm 2.17$	$32.79 \pm 2.58$	$39.55 \pm 3.08$
	RMSE	$22.34 \pm 1.55$	$15.72 \pm 1.54$	$14.35 \pm 1.66$	$25.19 \pm 3.65$	$32.67 \pm 11.24$	$14.98 \pm 5.06$
	SSIM	$0.8963 \pm 0.02$	$0.9594 \pm 0.01$	$0.9593 \pm 0.02$	$0.9354 \pm 0.02$	$0.9021 \pm 0.03$	$0.9563 \pm 0.02$
$10^4$	PSNR	$30.23 \pm 2.22$	$34.21 \pm 2.31$	$36.75 \pm 2.22$	$33.27 \pm 2.08$	$32.32 \pm 2.57$	$38.20 \pm 2.50$
	RMSE	$42.60 \pm 5.74$	$26.97 \pm 4.01$	$20.07 \pm 2.38$	$29.98 \pm 3.77$	$34.39 \pm 11.37$	$17.26 \pm 4.60$
	SSIM	$0.6883 \pm 0.06$	$0.8645 \pm 0.05$	$0.9275 \pm 0.02$	$0.8736 \pm 0.03$	$0.8912 \pm 0.03$	$0.9532 \pm 0.02$
$5 \times 10^3$	PSNR	$26.77 \pm 2.32$	$30.42 \pm 2.43$	$35.28 \pm 2.23$	$32.16 \pm 2.07$	$32.18 \pm 2.51$	$36.93 \pm 2.42$
	RMSE	$63.63 \pm 10.38$	$41.94 \pm 7.83$	$23.77 \pm 2.87$	$34.07 \pm 4.05$	$34.81 \pm 10.59$	$19.84 \pm 3.95$
	SSIM	$0.5401 \pm 0.07$	$0.7178 \pm 0.08$	$0.9123 \pm 0.03$	$0.8017 \pm 0.04$	$0.8861 \pm 0.03$	$0.9447 \pm 0.02$

- Neumann-Net<sup>21</sup> is proposed for linear inverse problem in generic imaging. Neumann-Net rolls the following iterative scheme:

$$\mathbf{x}^k = \mathbf{x}^{k-1} + \eta(\mathbf{I} - \eta \mathbf{A}^\top \mathbf{A})\mathbf{x}^{k-1} - \eta \mathcal{D}_{\text{cnn}}(\mathbf{x}^{k-1}; \theta^k),$$

where  $\mathcal{D}_{\text{cnn}}$  is a CNN-based mapping.

## V. RESULTS

In this section the proposed AHP-Net is evaluated on the simulated prostate CT data.

### V.A. Quantitative comparison on dataset

Three metrics, peak signal to noise ratio (PSNR), root mean square error (RMSE) and structural similarity index measure (SSIM)<sup>47</sup>, are used for quantitative evaluation of image quality. Recall that PSNR is defined as

$$\text{PSNR}(\mathbf{x}, \mathbf{x}^*) = -10 \log_{10} \left( \frac{\|\mathbf{x} - \mathbf{x}^*\|_2^2}{\max_i |x_i|^2} \right),$$

where  $\mathbf{x}^*$  denotes reconstructed image and  $\mathbf{x}$  denotes ground truth, i.e. normal dose image. RMSE is defined as  $\text{RMSE} = \sqrt{\frac{\sum_{i=1}^N (x_i^* - x_i)^2}{N}}$ , where  $N$  is the number of pixels.

See Table I for the quantitative comparison of the results from different methods, where different models are trained for processing the data w.r.t. different dose levels. It can be seen that the performance of two deep learning methods, MoDL and Neumann-Net, is noticeably worse than the other. One possible reason might be that MoDL is designed for MRI reconstruction and Neumann-Net for generic linear inverse problems. As a result, their network architectures might not fit the problem of LDCT reconstruction well. The proposed AHP-Net and FBPConvNet are two best performers among all methods. In the case of relatively high dose level,  $I_i = 10^5, 5 \times 10^4$ , the performances of these two methods are very close. In the case of relatively low dose level,  $I_i = 10^4, 5 \times 10^3$ , the proposed AHP-Net outperformed FBPConvNet by a noticeably margin, 1.5 – 1.8 dB advantage in PSNR.

See Table II for the quantitative comparison of the results from different methods, where one single model is trained for processing the data with varying dose levels. Again, MoDL and Neumann-Net did not perform as well as the others. The proposed AHP-Net is the best performer among all. The performance advantage of the proposed AHP-Net over the second best performer (FBPConvNet) is around 1dB for higher dose levels and 2dB for lower dose levels.

Indeed, when the performance of the universal model trained for varying dose levels is compared to that of the individual models trained for each fixed dose level. The proposed AHP-Net see the smallest performance hit, which ranges from 0.5 – 0.7dB in PSNR, in the case of low dose levels. Even so, by comparing Table I and Table II, the universal model of the AHP-Net still outperformed multiple models of other compared methods, in three tested dose levels:  $5 \times 10^4, 10^4, 5 \times 10^3$ .

In short, the proposed AHP-Net showed its advantage over existing representative non-learning methods and deep learning methods, specially when the dose level is low. Also, the proposed AHP has its advantage in terms of practical usage, as it allows to train a single model to processing the data w.r.t. varying dose levels with very competitive performance. The outcome of quantitative comparison clearly indicates the importance of the setting of hyper-parameters to optimization-unrolling-based deep learning methods and the effectiveness of our solution to it.

TABLE II: Quantitative comparison (Mean $\pm$ STD) of the results reconstructed by different methods on testing dataset, where one single model is trained for different dose levels in deep learning methods.

Dose level	Index	FBP	TV	FBPConvNet	MoDL	Neumann-Net	Our AHP-Net
$10^5$	PSNR	$37.15 \pm 2.04$	$39.75 \pm 2.18$	$39.92 \pm 2.03$	$35.06 \pm 2.12$	$33.27 \pm 2.62$	$40.54 \pm 2.42$
	RMSE	$19.06 \pm 1.10$	$14.18 \pm 1.38$	$13.90 \pm 1.33$	$24.50 \pm 3.80$	$30.93 \pm 10.84$	$13.15 \pm 2.97$
	SSIM	$0.9336 \pm 0.01$	$0.9685 \pm 0.01$	$0.9596 \pm 0.01$	$0.9434 \pm 0.02$	$0.9079 \pm 0.03$	$0.9703 \pm 0.01$
$5 \times 10^4$	PSNR	$35.78 \pm 2.05$	$38.85 \pm 2.18$	$39.18 \pm 2.07$	$34.94 \pm 2.12$	$33.24 \pm 2.62$	$40.07 \pm 2.40$
	RMSE	$22.34 \pm 1.55$	$15.72 \pm 1.54$	$15.14 \pm 1.45$	$24.82 \pm 3.77$	$31.03 \pm 10.83$	$13.85 \pm 2.96$
	SSIM	$0.8963 \pm 0.02$	$0.9594 \pm 0.01$	$0.9526 \pm 0.01$	$0.9366 \pm 0.02$	$0.9071 \pm 0.03$	$0.9670 \pm 0.01$
$10^4$	PSNR	$30.23 \pm 2.22$	$34.21 \pm 2.31$	$36.15 \pm 2.21$	$33.82 \pm 2.07$	$32.96 \pm 2.59$	$37.92 \pm 2.37$
	RMSE	$42.60 \pm 5.74$	$26.97 \pm 4.01$	$21.48 \pm 2.33$	$28.17 \pm 3.60$	$31.97 \pm 10.77$	$17.65 \pm 3.14$
	SSIM	$0.6883 \pm 0.06$	$0.8645 \pm 0.05$	$0.9199 \pm 0.02$	$0.8759 \pm 0.03$	$0.8995 \pm 0.03$	$0.9484 \pm 0.02$
$5 \times 10^3$	PSNR	$26.77 \pm 2.32$	$30.42 \pm 2.43$	$34.08 \pm 2.29$	$32.22 \pm 2.10$	$32.57 \pm 2.56$	$36.39 \pm 2.38$
	RMSE	$63.63 \pm 10.38$	$41.94 \pm 7.83$	$27.32 \pm 3.62$	$33.78 \pm 3.96$	$33.35 \pm 10.70$	$21.03 \pm 3.59$
	SSIM	$0.5401 \pm 0.07$	$0.7178 \pm 0.08$	$0.8862 \pm 0.04$	$0.7947 \pm 0.04$	$0.8879 \pm 0.03$	$0.9312 \pm 0.03$

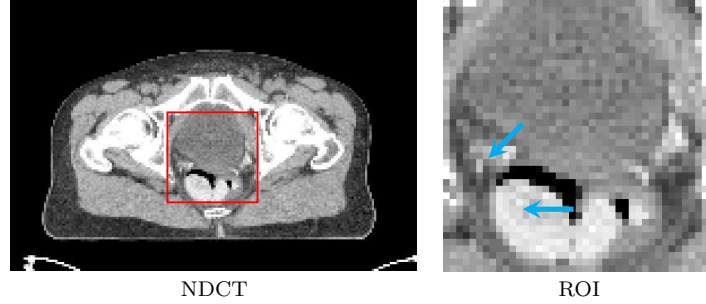


FIG. 4: Normal dose CT image and zoomed region (ROI).

### V.B. Visual comparison of some examples

Due to space limitation, only the images reconstructed by different methods from one sample measurement are shown for visual comparison. The dose level of the measurement is  $I_i = 10^4$ . The displayed window is set to  $[-150, 150]$  HU for all figures. More results w.r.t. other dose levels can be found in supplementary materials for visual comparison.

Fig. 4 demonstrates the selected normal dose CT (NDCT) image and the zoomed region of interesting (ROI). For the image reconstructed by the non-learning methods and the NN models trained by deep learning methods, specifically for the dose level  $I_i = 10^4$ , Fig. 5 shows the images reconstructed by different methods, and their zoomed-in images of boxes in Fig. 4 are displayed in Fig. 6. As shown by the cyan arrows, in comparison to the zoomed-in NDCT image, the results of FBPConvNet, MoDL and Neumann-Net were more blurred than that of the proposed method. See Table III for quantitative comparison of the results shown in Fig. 5.

For the image reconstructed by the non-learning methods and the universal NN model trained by deep learning methods for varying dose levels, specifically for the dose level  $I_i = 5 \times 10^3$ , Fig. 7 shows the images reconstructed by different methods, and their zoomed-in images of boxes in Fig. 4 are displayed in Fig. 8. As shown by the cyan arrows, in comparison to the zoomed-in NDCT image, the results of FBPConvNet, MoDL and Neumann-Net were more blurred than that of the proposed method. See Table III for quantitative comparison for the results shown in Fig. 7.

TABLE III: Quantitative metrics on the reconstruction results for the image slice shown in Fig. 5 and Fig. 7.

Method	FBP	TV	FBPConv Net	MoDL	Neumann-Net	Our AHP-Net
Fig. 5	PSNR	28.31	31.65	33.22	29.84	28.89
	RMSE	40.03	27.24	22.74	33.552	37.43
	SSIM	0.7204	0.8686	0.9040	0.8494	0.8376
Fig. 7	PSNR	25.12	28.09	31.66	29.17	29.12
	RMSE	57.78	41.06	27.20	36.27	36.47
	SSIM	0.5903	0.7342	0.8798	0.7731	0.8399

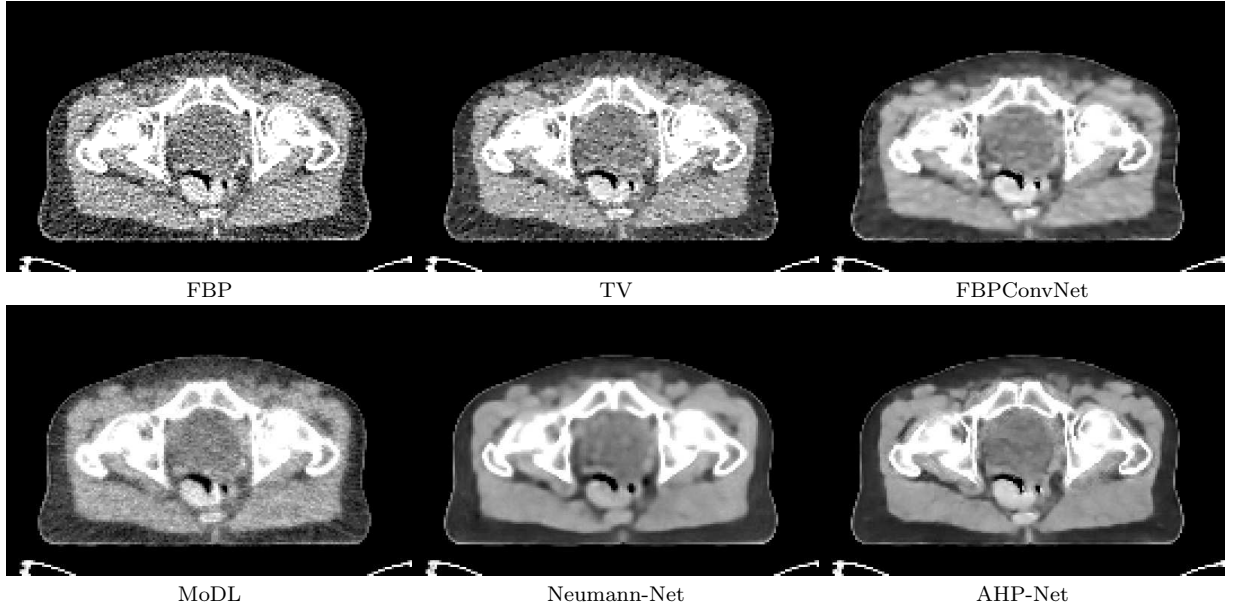


FIG. 5: Reconstruction results at dose level  $I_i = 10^4$  by the models trained under same dose level.

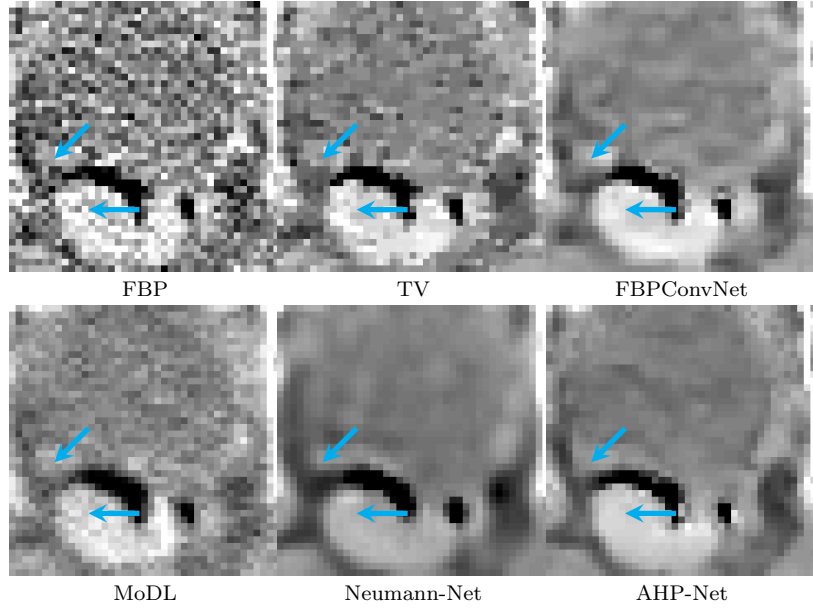


FIG. 6: Zoom-in results of Fig. 5 corresponding to the red boxes in Fig. 4.

### V.C. Ablation study

The ablation study conducted in this section focuses on how the following two parts impact the performance of image reconstruction: (1) the introduction of an MLP for adaptive prediction of the hyper-parameters and (2) the usages of 8 high-pass filters from Linear spline framelet. Through the whole ablation study, all different versions of the AHP-Net are trained by the same procedure on the same training/validation dataset and are tested on the same testing dataset. Different dose levels are trained with different models. See Table IV for the results from the different versions.

- $\nabla$  vs spline framelet filter bank. The results from the proposed AHP-Net are compared to that from the same NN but whose 8 framelet filters are replaced by 2 filters of  $\nabla$  ( $[1, -1], [1, -1]^T$ ) seen in TV regularization. See the comparison of the column titled as “Using  $\nabla$ ” and that titled as “AHP-Net” in Table IV. The results under

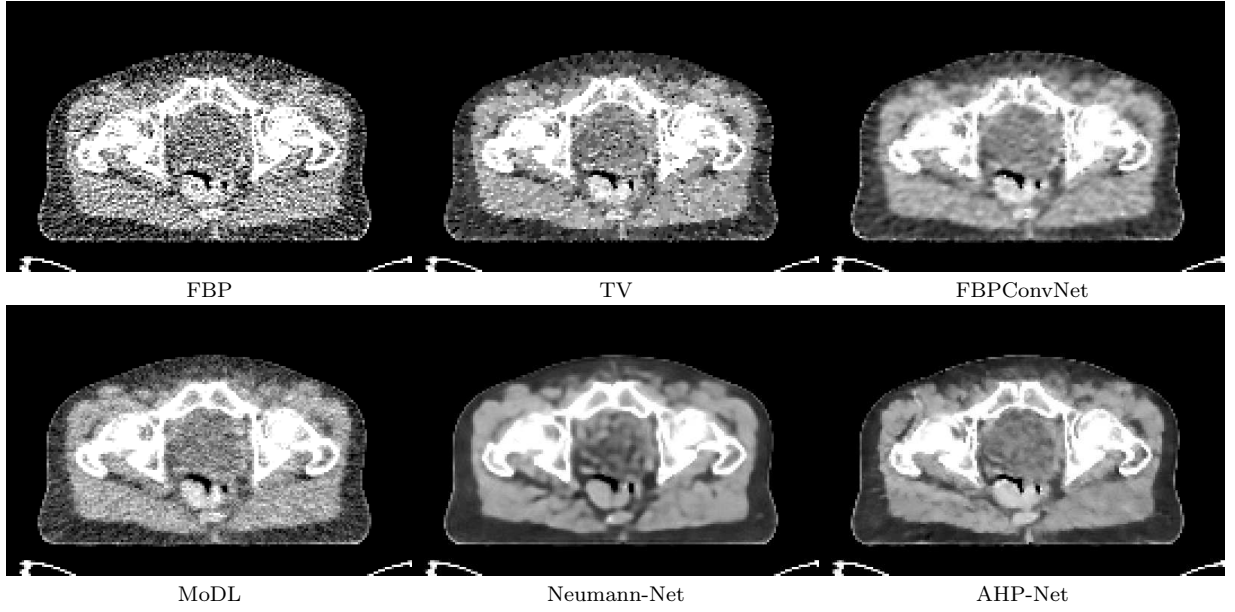


FIG. 7: Reconstruction results at dose level  $I_i = 5 \times 10^3$  by the universal models trained for varying dose levels.

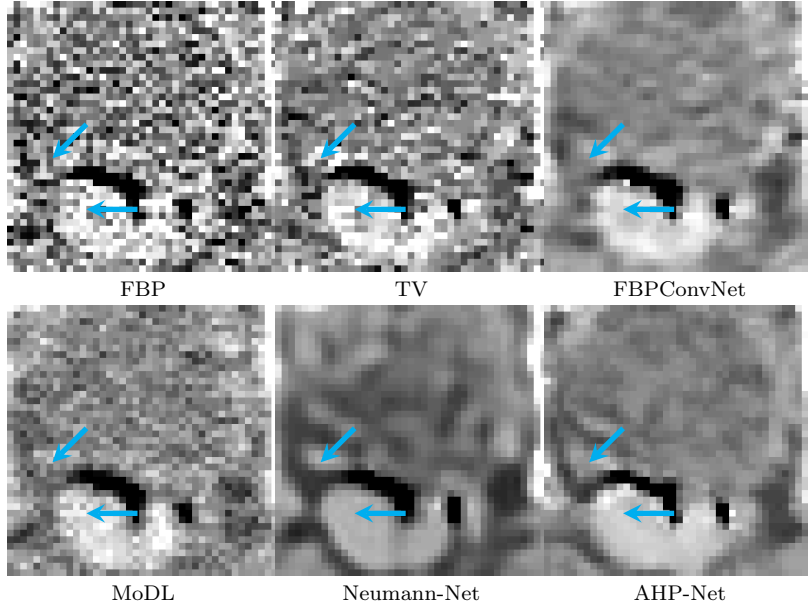


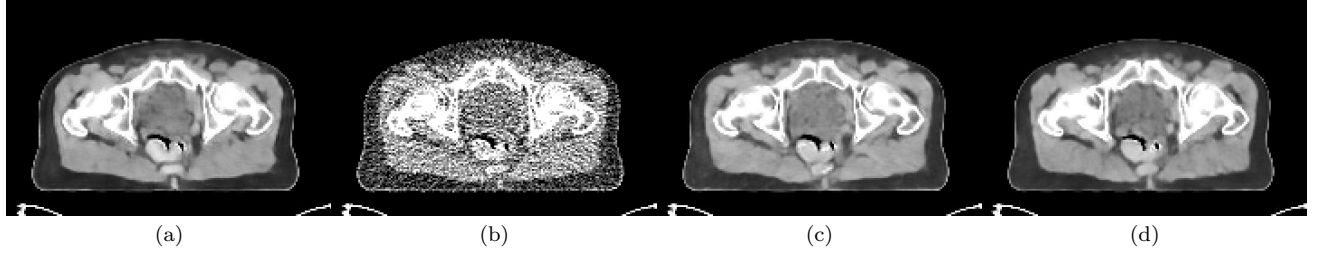
FIG. 8: Zoom-in results of Fig. 7 corresponding to the red boxes in Fig. 4.

different dose level showed the advantage of 8 filters over gradient operator  $\nabla$ , about 1.2 – 1.9 dB in PSNR. It is noted that in addition to performance gain by using the framelet filter bank, the performance benefit brought by MLP-based predictor is also fully exploited when using  $\nabla$ , as only 2 parameters are involved when using  $\nabla$ .

- *Learnable filters vs Spline framelet filter bank.* The results from the proposed AHP-Net are compared to that from the same NN but whose 8 filters are treated as network parameters learned on training dataset; see the column titled as “Learnable filters” in Table IV. Surprisingly, learnable filter bank only performed better than gradient operator  $\nabla$  in the case of higher dose level. In the case of lower dose level, there is a significant performance hit when using learnable filter banks over  $\nabla$ . One possible cause is that network training needs to solve a highly non-convex optimization problem with millions of network parameters. The filter bank plays an important role in the performance of the NN. However, when they are treated as one part of network parameters, they do not receive sufficient attention in the training.

TABLE IV: Quantitative comparison (Mean $\pm$ STD) of the results reconstructed by the different versions of the AHP-Net for ablation study

Dose level	Index	Using $\nabla$	Learnable filters	Learnable HP	AHP-Net
$10^5$	PSNR	$39.26 \pm 2.86$	$37.15 \pm 2.03$	$40.86 \pm 2.54$	$41.12 \pm 2.69$
	RMSE	$15.46 \pm 4.62$	$19.06 \pm 1.10$	$12.80 \pm 4.10$	$12.41 \pm 3.31$
	SSIM	$0.9656 \pm 0.01$	$0.9336 \pm 0.01$	$0.9686 \pm 0.02$	$0.9739 \pm 0.01$
$5 \times 10^4$	PSNR	$38.41 \pm 2.98$	$35.78 \pm 2.05$	$39.03 \pm 3.11$	$39.55 \pm 3.08$
	RMSE	$17.25 \pm 7.16$	$22.33 \pm 1.55$	$16.14 \pm 7.24$	$14.98 \pm 5.06$
	SSIM	$0.9566 \pm 0.02$	$0.8963 \pm 0.02$	$0.9618 \pm 0.02$	$0.9563 \pm 0.02$
$10^4$	PSNR	$36.91 \pm 2.49$	$30.23 \pm 2.22$	$36.78 \pm 2.42$	$38.20 \pm 2.50$
	RMSE	$19.98 \pm 4.51$	$42.59 \pm 5.73$	$20.14 \pm 3.59$	$17.26 \pm 4.60$
	SSIM	$0.9383 \pm 0.02$	$0.6883 \pm 0.06$	$0.9368 \pm 0.02$	$0.9532 \pm 0.02$
$5 \times 10^3$	PSNR	$35.08 \pm 3.31$	$26.77 \pm 2.32$	$35.63 \pm 2.49$	$36.85 \pm 1.85$
	RMSE	$26.21 \pm 19.65$	$63.66 \pm 10.37$	$23.08 \pm 5.19$	$36.93 \pm 2.42$
	SSIM	$0.9191 \pm 0.05$	$0.5399 \pm 0.07$	$0.9229 \pm 0.03$	$0.9447 \pm 0.02$

FIG. 9: Reconstruction results at dose level  $I_i = 5 \times 10^3$  by the models trained under same dose level. (a) Using  $\nabla$ ; (b) Learnable filters  $\{F_i\}$ ; (c) Learnable HP; (d) AHP-net.

- *Learning constant hyper-parameters as network weights vs Using an MLP for adaptive prediction of hyper-parameters.* The results from the proposed AHP-Net are compared to that from the same NN but whose hyper-parameters  $\{\beta_j^k\}$  are treated as network parameters learned on training dataset; see the column titled as “Learnable HP” in Table IV. In the case of higher dose levels,  $I_i = 10^5, 5 \times 10^4$ , the performance gain of learning an MLP for adaptive prediction of hyper-parameters is about 0.3 – 0.5dB in PSNR. In the case of lower dose levels,  $I_i = 10^4, 5 \times 10^3$ , there is a significant improvement of MLP-based adaptive prediction over learnable constant hyper-parameters, about 1.3 – 1.4dB in PSNR.

See Fig. 9 for the visual comparison of the results by the different versions of the AHP-Net trained under same dose level reconstructed from some example with dose level  $I_i = 5 \times 10^3$ , and Fig. 10 for their zoomed-in regions of the boxes in Fig. 4. Please see supplementary materials for visual comparison of more examples.

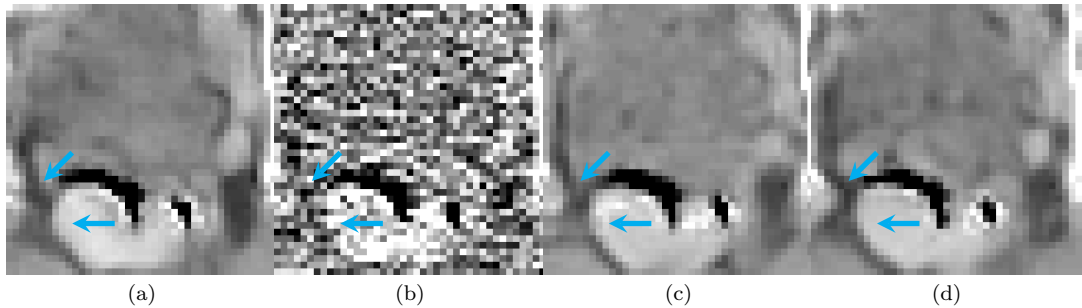
FIG. 10: Zoom-in results of Fig. 9 corresponding to the red boxes in Fig. 4. (a) Using  $\nabla$ ; (b) Learnable filters  $\{F_i\}$ ; (c) Learnable HP; (d) AHP-net.

TABLE V: Cross-validation Quantitative results of one single model trained for different dose levels.

Dose level	Method		Fold 1	Fold 2	Fold 3	Fold 4	Fold 5	Mean $\pm$ STD
$10^5$	FBPConvNet	PSNR	39.27	39.15	39.01	39.55	39.92	39.39 $\pm$ 0.36
		RMSE	14.57	14.39	14.60	13.76	13.90	14.25 $\pm$ 0.39
		SSIM	0.9583	0.9564	0.9549	0.9600	0.9596	0.9578 $\pm$ 0.00
	AHP-Net	PSNR	39.68	40.24	39.40	40.06	40.54	39.98 $\pm$ 0.45
		RMSE	15.57	13.24	14.43	13.19	13.15	13.92 $\pm$ 1.07
		SSIM	0.9660	0.9507	0.9569	0.9555	0.9703	0.9210 $\pm$ 0.01
$5 \times 10^4$	FBPConvNet	PSNR	38.45	38.80	38.02	38.65	39.18	38.52 $\pm$ 0.44
		RMSE	16.01	15.90	16.18	15.26	15.14	15.70 $\pm$ 0.47
		SSIM	0.9485	0.9458	0.9446	0.9506	0.9526	0.9371 $\pm$ 0.00
	AHP-Net	PSNR	39.30	38.29	39.02	39.72	40.07	39.58 $\pm$ 0.42
		RMSE	16.15	13.87	15.02	13.69	13.85	14.52 $\pm$ 1.06
		SSIM	0.9624	0.9474	0.9538	0.9443	0.9670	0.9371 $\pm$ 0.01
$10^4$	FBPConvNet	PSNR	35.45	35.53	35.27	35.69	36.15	35.62 $\pm$ 0.33
		RMSE	22.59	21.85	22.73	21.50	21.48	22.03 $\pm$ 0.60
		SSIM	0.9096	0.9124	0.9082	0.9169	0.9199	0.9134 $\pm$ 0.01
	AHP-Net	PSNR	37.31	37.59	37.21	37.95	37.92	37.59 $\pm$ 0.34
		RMSE	19.72	17.60	18.38	16.70	17.65	18.01 $\pm$ 1.13
		SSIM	0.9425	0.9288	0.9367	0.9289	0.9484	0.9550 $\pm$ 0.01
$5 \times 10^3$	FBPConvNet	PSNR	33.62	33.55	33.34	33.91	34.08	33.70 $\pm$ 0.30
		RMSE	27.91	27.53	28.43	26.41	24.72	27.52 $\pm$ 0.75
		SSIM	0.8783	0.8771	0.8761	0.8888	0.9005	0.8813 $\pm$ 0.06
	AHP-Net	PSNR	35.72	36.03	35.87	36.57	36.39	36.12 $\pm$ 0.36
		RMSE	23.57	20.97	21.40	19.54	21.03	21.30 $\pm$ 1.45
		SSIM	0.9234	0.9123	0.9222	0.9157	0.9312	0.9582 $\pm$ 0.01

#### V.D. Cross-validation

For great computational cost of training a network, in this section, a  $k$ -fold cross-validation is conducted on the proposed AHP-Net and the second best deep learning method, FBPConvNet, in the previous experiments, to give a comprehensive measure of two methods' performance throughout the whole dataset. More specifically, 100 scans are equally partitioned into 5 folders. Then, for each folder, the images associated with the scans from this fold are used for testing, and all others are used for training. One single model is trained for different noise levels. See Table V for the list of average quantitative metric values of the results from two methods on each test dataset. It can be seen the proposed AHP-Net consistently outperformed FBPConvNet, and the performance margin is quite noticeable when the dose level is low.

## VI. DISCUSSION AND CONCLUSION

Similarly to many optimization-unrolling-based deep learning methods, this paper also proposed a deep learning method for LDCT image reconstruction, the AHP-Net, that unrolls the half-quadratic splitting scheme for MBIR. Each stage of the AHP-Net contains one inversion block and a denoising block, where the denoising block is built-on a CNN. The main difference of the proposed AHP-Net from other deep learning solutions lies the design of the inversion block.

In the proposed inversion block, we replaced the often-used gradient operator  $\nabla$  by the filter banks with 8 high-pass filters from linear spline framelet transform, motivated by its success in  $\ell_1$ -norm relating regularization in image recovery. Moreover, we proposed to pay special attention to the hyper-parameters involved in the inversion block, and presented a MLP-based NN to predict hyper-parameters that adaptive to both dose level and image content.

The experiments showed the advantage of the proposed method over classic non-learning methods and some representative deep learning based methods for LDCT reconstruction. Also, another advantage is that the proposed method can only train a single model with competitive performance to process measurement data with varying dose levels.

As different dose levels implicitly refers to different SNRs. The proposed methods indeed allows to train a universal model with competitive performance to process the data with unknown SNRs, which can be valuable to practical applications in medical CT imaging. In practical medical CT scans, the dose level is not fixed and the SNR of the data is also different for different people under the same dose level, *e.g.* adult vs child. The adaptivity of the proposed method to different SNRs of data can be welcomed in practice.

There still exist some issues in the proposed method. One is that the squared  $\ell_2$ -norm  $\|\cdot\|_2^2$  is used the proposed methods, which is sub-optimal to the weighted squared  $\ell_2$ -norm  $\|\text{diag}(\mathbf{w}) \cdot \|\cdot\|_2^{2,23}$ , specially in the case of ultra-low dose CT. Although, our approach can also use  $\|\text{diag}(\mathbf{w}) \cdot \|\cdot\|_2^2$  without any technical obstacle. It remains a challenging



task to accurately estimate such a  $\text{diag}(\mathbf{w})$  w.r.t. varying dose levels. Another issue is that instead of reconstructing the 3D volume as a whole, the proposed method separately reconstructs image slices. The main reason we take such a reconstruction scheme is that the number of network parameters of the NN adopted in this paper will increase exponentially when constructing the whole 3D volume. The resulting memory usage in GPU will be too excessive to make the computation feasible under current available commodity GPUs.

In future work, we will study how to further improve the reconstruction by merging the estimation the weighting matrix  $\text{diag}(\mathbf{w})$  in the fidelity term for better treatment on noise, and study how to design compact deep NN that can directly reconstruct 3D volume in LDCT image reconstruction. Also, we will investigate the applications of the proposed method in other medical image reconstruction problems, *e.g.* sparse-view CT reconstruction and image reconstruction from sparse samples in MRI.

a) [matding@nus.edu.sg](mailto:matding@nus.edu.sg), [nanyuesong@u.nus.edu](mailto:nanyuesong@u.nus.edu), [matjh@nus.edu.sg](mailto:matjh@nus.edu.sg)

b) [hao.gao.2012@gmail.com](mailto:hao.gao.2012@gmail.com)

- <sup>1</sup>Jonas Adler and Ozan Öktem. Learned primal-dual reconstruction. *IEEE transactions on medical imaging*, 37(6):1322–1332, 2018.
- <sup>2</sup>Hemant K Aggarwal, Merry P Mani, and Mathews Jacob. MoDL: Model-based deep learning architecture for inverse problems. *IEEE transactions on medical imaging*, 38(2):394–405, 2018.
- <sup>3</sup>Ti Bai, Hao Yan, Xun Jia, Steve Jiang, Ge Wang, and Xuanqin Mou. Z-index parameterization for volumetric CT image reconstruction via 3-D dictionary learning. *IEEE transactions on medical imaging*, 36(12):2466–2478, 2017.
- <sup>4</sup>Shabab Bazrafkan, Vincent Van Nieuwenhove, Joris Soons, Jan De Beenhouwer, and Jan Sijbers. Deep neural network assisted iterative reconstruction method for low dose CT. *arXiv preprint arXiv:1906.00650*, 2019.
- <sup>5</sup>Jianfeng Cai, Xun Jia, Hao Gao, Steve B Jiang, Zuowei Shen, and Hongkai Zhao. Cine cone beam CT reconstruction using low-rank matrix factorization: algorithm and a proof-of-principle study. *IEEE transactions on medical imaging*, 33(8):1581–1591, 2014.
- <sup>6</sup>Guanghong Chen and Yinsheng Li. Synchronized multiartifact reduction with tomographic reconstruction (SMART-RECON): A statistical model based iterative image reconstruction method to eliminate limited-view artifacts and to mitigate the temporal-average artifacts in time-resolved CT. *Medical physics*, 42(8):4698–4707, 2015.
- <sup>7</sup>Guanghong Chen, Jie Tang, and Shuai Leng. Prior image constrained compressed sensing (PICCS): a method to accurately reconstruct dynamic CT images from highly undersampled projection data sets. *Medical physics*, 35(2):660–663, 2008.
- <sup>8</sup>Hu Chen, Yi Zhang, Yunjin Chen, Junfeng Zhang, Weihua Zhang, Huaiqiang Sun, Yang Lv, Peixi Liao, Jiliu Zhou, and Ge Wang. LEARN: Learned experts’ assessment-based reconstruction network for sparse-data CT. *IEEE transactions on medical imaging*, 37(6):1333–1347, 2018.
- <sup>9</sup>Hu Chen, Yi Zhang, Mannudeep K Kalra, Feng Lin, Yang Chen, Peixi Liao, Jiliu Zhou, and Ge Wang. Low-dose CT with a residual encoder-decoder convolutional neural network. *IEEE transactions on medical imaging*, 36(12):2524–2535, 2017.
- <sup>10</sup>Hu Chen, Yi Zhang, Weihua Zhang, Peixi Liao, Ke Li, Jiliu Zhou, and Ge Wang. Low-dose CT via convolutional neural network. *Biomedical optics express*, 8(2):679–694, 2017.
- <sup>11</sup>Andrew R Conn, Nicholas IM Gould, and Philippe Toint. A globally convergent augmented lagrangian algorithm for optimization with general constraints and simple bounds. *SIAM Journal on Numerical Analysis*, 28(2):545–572, 1991.
- <sup>12</sup>Qiaoqiao Ding, Gaoyu Chen, Xiaoqun Zhang, Qiu Huang, Hui Ji, and Hao Gao. Low-dose ct with deep learning regularization via proximal forward backward splitting. *Physics in Medicine & Biology*, 2020.
- <sup>13</sup>Qiaoqiao Ding, Yong Long, Xiaoqun Zhang, and Jeffrey A Fessler. Modeling mixed poisson-gaussian noise in statistical image reconstruction for x-ray ct. *Arbor*, 1001:48109, 2016.
- <sup>14</sup>Qiaoqiao Ding, Yong Long, Xiaoqun Zhang, and Jeffrey A Fessler. Statistical image reconstruction using mixed poisson-gaussian noise model for X-ray CT. *arXiv preprint arXiv:1801.09533*, 2018.
- <sup>15</sup>Bin Dong, Zuowei Shen, et al. MRA based wavelet frames and applications. *IAS Lecture Notes Series, Summer Program on 'The Mathematics of Image Processing', Park City Mathematics Institute*, 19, 2010.
- <sup>16</sup>Jeffrey A Fessler. Statistical image reconstruction methods for transmission tomography. *Handbook of medical imaging*, 2:1–70, 2000.
- <sup>17</sup>Hao Gao, Jianfeng Cai, Zuowei Shen, and Hongkai Zhao. Robust principal component analysis-based four-dimensional computed tomography. *Physics in Medicine & Biology*, 56(11):3181, 2011.
- <sup>18</sup>Hao Gao, Ruijiang Li, Yuting Lin, and Lei Xing. 4D cone beam CT via spatiotemporal tensor framelet. *Medical physics*, 39(11):6943–6946, 2012.
- <sup>19</sup>Hao Gao, Hengyong Yu, Stanley Osher, and Ge Wang. Multi-energy CT based on a prior rank, intensity and sparsity model (PRISM). *Inverse problems*, 27(11):115012, 2011.
- <sup>20</sup>Donald Geman and Chengda Yang. Nonlinear image recovery with half-quadratic regularization. *IEEE transactions on Image Processing*, 4(7):932–946, 1995.
- <sup>21</sup>Davis Gilton, Greg Ongie, and Rebecca Willett. Neumann networks for inverse problems in imaging. *arXiv preprint arXiv:1901.03707*, 2019.
- <sup>22</sup>Gene H Golub, Michael Heath, and Grace Wahba. Generalized cross-validation as a method for choosing a good ridge parameter. *Technometrics*, 21(2):215–223, 1979.
- <sup>23</sup>Harshit Gupta, Kyong Hwan Jin, Ha Q Nguyen, Michael T McCann, and Michael Unser. CNN-based projected gradient descent for consistent CT image reconstruction. *IEEE transactions on medical imaging*, 37(6):1440–1453, 2018.
- <sup>24</sup>Yo Seob Han, Jaejun Yoo, and Jong Chul Ye. Deep residual learning for compressed sensing CT reconstruction via persistent homology analysis. *arXiv preprint arXiv:1611.06391*, 2016.
- <sup>25</sup>Per Christian Hansen. Analysis of discrete ill-posed problems by means of the L-curve. *SIAM review*, 34(4):561–580, 1992.
- <sup>26</sup>Andreas Hauptmann, Felix Lucka, Marta Betcke, Nam Huynh, Jonas Adler, Ben Cox, Paul Beard, Sebastien Ourselin, and Simon Arridge. Model-based learning for accelerated, limited-view 3-d photoacoustic tomography. *IEEE transactions on medical imaging*, 37(6):1382–1393, 2018.
- <sup>27</sup>Ji He, Yan Yang, Yongbo Wang, Dong Zeng, Zhaoying Bian, Hao Zhang, Jian Sun, Zongben Xu, and Jianhua Ma. Optimizing a parameterized plug-and-play ADMM for iterative low-dose CT reconstruction. *IEEE transactions on medical imaging*, 38(2):371–382, 2018.
- <sup>28</sup>Gao Huang, Zhuang Liu, Laurens Van Der Maaten, and Kilian Q Weinberger. Densely connected convolutional networks. In *Proceedings of the IEEE conference on computer vision and pattern recognition*, pages 4700–4708, 2017.

- <sup>29</sup>Xun Jia, Bin Dong, Yifei Lou, and Steve B Jiang. GPU-based iterative cone-beam CT reconstruction using tight frame regularization. *Physics in Medicine & Biology*, 56(13):3787, 2011.
- <sup>30</sup>Xun Jia, Yifei Lou, Bin Dong, Zhen Tian, and Steve Jiang. 4D computed tomography reconstruction from few-projection data via temporal non-local regularization. In *International Conference on Medical Image Computing and Computer-Assisted Intervention*, pages 143–150. Springer, 2010.
- <sup>31</sup>Bangti Jin, Yubo Zhao, and Jun Zou. Iterative parameter choice by discrepancy principle. *IMA Journal of Numerical Analysis*, 32(4):1714–1732, 2012.
- <sup>32</sup>Kyong Hwan Jin, Michael T McCann, Emmanuel Froustey, and Michael Unser. Deep convolutional neural network for inverse problems in imaging. *IEEE Transactions on Image Processing*, 26(9):4509–4522, 2017.
- <sup>33</sup>Eunhee Kang, Junhong Min, and Jong Chul Ye. A deep convolutional neural network using directional wavelets for low-dose X-ray CT reconstruction. *Medical physics*, 44(10):e360–e375, 2017.
- <sup>34</sup>Eunhee Kang, Jong Chul Ye, et al. Wavelet domain residual network (WavResNet) for low-dose X-ray CT reconstruction. *arXiv preprint arXiv:1703.01383*, 2017.
- <sup>35</sup>Heyi Li and Klaus Mueller. Low-dose CT streak artifacts removal using deep residual neural network. In *Proc. Fully Three-Dimensional Image Reconstruction Radiol. Nucl. Med. (Fully3D)*, pages 191–194, 2017.
- <sup>36</sup>Morteza Mardani, Hatef Monajemi, Vardan Papyan, Shreyas Vasanaawala, David Donoho, and John Pauly. Recurrent generative adversarial networks for proximal learning and automated compressive image recovery. *arXiv preprint arXiv:1711.10046*, 2017.
- <sup>37</sup>Johan Nuyts, Bruno De Man, Jeffrey A Fessler, Wojciech Zbijewski, and Freek J Beekman. Modelling the physics in the iterative reconstruction for transmission computed tomography. *Physics in medicine and biology*, 58(12):R63, 2013.
- <sup>38</sup>Adam Paszke, Sam Gross, Soumith Chintala, Gregory Chanan, Edward Yang, Zachary DeVito, Zeming Lin, Alban Desmaison, Luca Antiga, and Adam Lerer. Automatic differentiation in pytorch. 2017.
- <sup>39</sup>Daniel Maria Pelt and Kees Joost Batenburg. Fast tomographic reconstruction from limited data using artificial neural networks. *IEEE Transactions on Image Processing*, 22(12):5238–5251, 2013.
- <sup>40</sup>Sathish Ramani, Zhihao Liu, Jeffrey Rosen, Jon-Fredrik Nielsen, and Jeffrey A Fessler. Regularization parameter selection for nonlinear iterative image restoration and MRI reconstruction using GCV and SURE-based methods. *IEEE Transactions on Image Processing*, 21(8):3659–3672, 2012.
- <sup>41</sup>Ken D Sauer and Charles A Bouman. A local update strategy for iterative reconstruction from projections. *IEEE Transactions on Signal Processing*, 41(2):534–548, 1993.
- <sup>42</sup>Emil Y Sidky, Chien-Min Kao, and Xiaochuan Pan. Accurate image reconstruction from few-views and limited-angle data in divergent-beam ct. *Journal of X-ray Science and Technology*, 14(2):119–139, 2006.
- <sup>43</sup>Emil Y Sidky and Xiaochuan Pan. Image reconstruction in circular cone-beam computed tomography by constrained, total-variation minimization. *Physics in Medicine & Biology*, 53(17):4777, 2008.
- <sup>44</sup>Jian Sun, Huibin Li, Zongben Xu, et al. Deep ADMM-Net for compressive sensing MRI. In *Advances in neural information processing systems*, pages 10–18, 2016.
- <sup>45</sup>Jean-Baptiste Thibault, Ken D Sauer, Charles A Bouman, and Jiang Hsieh. A three-dimensional statistical approach to improved image quality for multislice helical CT. *Medical physics*, 34(11):4526–4544, 2007.
- <sup>46</sup>Yu Wang, Wotao Yin, and Jinshan Zeng. Global convergence of ADMM in nonconvex nonsmooth optimization. *Journal of Scientific Computing*, 78(1):29–63, 2019.
- <sup>47</sup>Zhou Wang, Alan C Bovik, Hamid R Sheikh, Eero P Simoncelli, et al. Image quality assessment: from error visibility to structural similarity. *IEEE transactions on image processing*, 13(4):600–612, 2004.
- <sup>48</sup>Bruce R Whiting, Parinaz Massoumzadeh, Orville A Earl, Joseph A O Sullivan, Donald L Snyder, and Jeffrey F Williamson. Properties of preprocessed sinogram data in X-ray computed tomography. *Medical physics*, 33(9):3290–3303, 2006.
- <sup>49</sup>Jelmer M Wolterink, Tim Leiner, Max A Viergever, and Ivana Išgum. Generative adversarial networks for noise reduction in low-dose CT. *IEEE transactions on medical imaging*, 36(12):2536–2545, 2017.
- <sup>50</sup>Dufan Wu, Kyungsang Kim, Georges El Fakhri, and Quanzheng Li. Iterative low-dose CT reconstruction with priors trained by artificial neural network. *IEEE transactions on medical imaging*, 36(12):2479–2486, 2017.
- <sup>51</sup>Qiong Xu, Hengyong Yu, Xuanqin Mou, Lei Zhang, Jiang Hsieh, and Ge Wang. Low-dose X-ray CT reconstruction via dictionary learning. *IEEE transactions on medical imaging*, 31(9):1682–1697, 2012.
- <sup>52</sup>Qingsong Yang, Pingkun Yan, Yanbo Zhang, Hengyong Yu, Yongyi Shi, Xuanqin Mou, Mannudeep K Kalra, Yi Zhang, Ling Sun, and Ge Wang. Low-dose CT image denoising using a generative adversarial network with wasserstein distance and perceptual loss. *IEEE transactions on medical imaging*, 37(6):1348–1357, 2018.
- <sup>53</sup>Jong Chul Ye, Yoseob Han, and Eunju Cha. Deep convolutional framelets: A general deep learning framework for inverse problems. *SIAM Journal on Imaging Sciences*, 11(2):991–1048, 2018.
- <sup>54</sup>Xiaoqun Zhang and Jacques Froment. Total variation based fourier reconstruction and regularization for computer tomography. In *Nuclear Science Symposium Conference Record, 2005 IEEE*, volume 4, pages 2332–2336. IEEE, 2005.

# AHP-Net: adaptive-hyper-parameter deep learning based image reconstruction method for multilevel low-dose CT: Supplementary Materials

In this supplementary file, we provide the following materials

- The details of calculating the gradients of the loss function w.r.t. all parameters, using back-propagation over the deep architecture in Fig. 3.
- The details of the implementation and training of comparison methods
- Visual comparison on more examples.

## I. BACK-PROPAGATION

During the train process, we need to calculate gradients about  $\Theta_k = \{\theta_D^{k-1}, \theta_P^k, \theta_I^k\}, k = 1, \dots, K$ . The loss of the proposed neural network is as follows,

$$\mathcal{L}(\Theta) = \frac{1}{J} \sum_{j=1}^J \left( \|\mathbf{x}_j^K - \mathbf{x}_j\|_2^2 + \sum_{k=1}^{K-1} \mu_k \|\mathbf{x}_j^k - \mathbf{x}_j\|_2^2 \right), \quad (1)$$

Recall that  $g^k(\mathbf{x}) = \mathbf{A}^\top(\mathbf{A}\mathbf{x} - \mathbf{y}) + \sum_{i=1}^L \beta_i^k \mathbf{F}_i^\top(\mathbf{F}_i\mathbf{x} - \mathbf{z}_i^k)$ , and  $\mathbf{x}_t^k = \mathbf{x}_{t-1}^k - \theta_{t-1}^k g^k(\mathbf{x}_{t-1}^k)$ , where  $\mathbf{x}_0^k = \mathbf{x}^{k-1}$  and  $\mathbf{x}^k = \mathbf{x}_T^k$ .

We give the details of the gradient calculation procedure. For simplify, we omit the data index  $j$ ,

$$\frac{\partial \mathcal{L}(\Theta)}{\partial \theta_t^k} = \frac{\partial \mathcal{L}(\Theta)}{\partial \mathbf{x}^k} \cdot \frac{\partial \mathbf{x}^k}{\partial \theta_t^k}, \quad (2)$$

$$\frac{\partial \mathcal{L}(\Theta)}{\partial \theta_P^k} = \frac{\partial \mathcal{L}(\Theta)}{\partial \mathbf{x}^k} \cdot \frac{\partial \mathbf{x}^k}{\partial \theta_P^k}, \quad (3)$$

$$\frac{\partial \mathcal{L}(\Theta)}{\partial \theta_D^{k-1}} = \frac{\partial \mathcal{L}(\Theta)}{\partial \mathbf{x}^k} \cdot \frac{\partial \mathbf{x}^k}{\partial \theta_D^{k-1}}, \quad (4)$$

where

$$\begin{aligned} \frac{\partial \mathcal{L}(\Theta)}{\partial \mathbf{x}^k} &= \mu_k \frac{\partial \|\mathbf{x}^k - \mathbf{x}\|_2^2}{\partial \mathbf{x}^k} + \mu_{k+1} \frac{\partial \|\mathbf{x}^{k+1} - \mathbf{x}\|_2^2}{\partial \mathbf{x}^{k+1}} \cdot \frac{\partial \mathbf{x}^{k+1}}{\partial \mathbf{x}^k} + \dots \\ &\quad + \mu_{K-1} \frac{\partial \|\mathbf{x}^{K-1} - \mathbf{x}\|_2^2}{\partial \mathbf{x}^{K-1}} \cdot \frac{\partial \mathbf{x}^{K-1}}{\partial \mathbf{x}^{K-2}} \dots \frac{\partial \mathbf{x}^{K-1}}{\partial \mathbf{x}^k} \\ &\quad + \frac{\partial \|\mathbf{x}^K - \mathbf{x}\|_2^2}{\partial \mathbf{x}^K} \cdot \frac{\partial \mathbf{x}^K}{\partial \mathbf{x}^{K-1}} \dots \frac{\partial \mathbf{x}^K}{\partial \mathbf{x}^k}, \end{aligned} \quad (5)$$

and

$$\left\{ \begin{array}{l} \frac{\partial \|\mathbf{x}^k - \mathbf{x}\|_2^2}{\partial \mathbf{x}^k} = 2(\mathbf{x}^k - \mathbf{x}), \quad (6a) \\ \frac{\partial \mathbf{x}^k}{\partial \mathbf{x}^{k-1}} = \frac{\partial \mathbf{x}_T^k}{\partial \mathbf{x}_0^k} = \frac{\partial \mathbf{x}_T^k}{\partial \mathbf{x}_{T-1}^k} \cdots \frac{\partial \mathbf{x}_t^k}{\partial \mathbf{x}_{t-1}^k} \cdots \frac{\partial \mathbf{x}_1^k}{\partial \mathbf{x}_0^k}, \quad (6b) \\ \frac{\partial \mathbf{x}_t^k}{\partial \mathbf{x}_{t-1}^k} = \mathbf{I} - \theta_{t-1}^k \frac{\partial g^k(\mathbf{x}_{t-1}^k)}{\partial \mathbf{x}_{t-1}^k}, \quad (6c) \\ \frac{\partial g^k(\mathbf{x}_{t-1}^k)}{\partial \mathbf{x}_{t-1}^k} = \mathbf{A}^\top \mathbf{A} + \sum_{i=1}^L \beta_i^k \mathbf{F}_i^\top \mathbf{F}_i, \quad (6d) \\ \frac{\partial \mathbf{x}^k}{\partial \theta_t^k} = \frac{\partial \mathbf{x}_T^k}{\partial \theta_t^k} = \frac{\partial \mathbf{x}_T^k}{\partial \mathbf{x}_{T-1}^k} \cdots \frac{\partial \mathbf{x}_{t+2}^k}{\partial \mathbf{x}_{t+1}^k} \cdot \frac{\partial \mathbf{x}_{t+1}^k}{\partial \theta_t^k}, \quad (6e) \\ \frac{\partial \mathbf{x}_{t+1}^k}{\partial \theta_t^k} = g^k(\mathbf{x}_t^k), \quad (6f) \\ \frac{\partial \mathbf{x}^k}{\partial \theta_{\mathcal{D}}^k} = \sum_{t=0}^{T-1} \frac{\partial \mathbf{x}_T^k}{\partial \mathbf{x}_{T-1}^k} \cdots \frac{\partial \mathbf{x}_{t+2}^k}{\partial \mathbf{x}_{t+1}^k} \cdot \frac{\partial \mathbf{x}_{t+1}^k}{\partial \theta_{\mathcal{D}}^k}, \quad (6g) \\ \frac{\partial \mathbf{x}_{t+1}^k}{\partial \theta_{\mathcal{D}}^k} = \frac{\partial \mathbf{x}_{t+1}^k}{\partial \mathbf{x}_t^k} \frac{\partial \mathbf{x}_t^k}{\partial \theta_{\mathcal{D}}^k} + \frac{\partial \mathbf{x}_{t+1}^k}{\partial \mathbf{z}^k} \frac{\partial \mathbf{z}^k}{\partial \tilde{\mathbf{x}}^{k-1}} \frac{\partial \tilde{\mathbf{x}}^{k-1}}{\partial \theta_{\mathcal{D}}^k}, \quad (6h) \\ \frac{\partial \mathbf{x}_{t+1}^k}{\partial \mathbf{z}_i^k} = \beta_i^k \mathbf{F}_i^\top, \quad (6i) \\ \frac{\partial \mathbf{z}_i^k}{\partial \tilde{\mathbf{x}}^{k-1}} = \mathbf{F}_i, \quad (6j) \\ \frac{\partial \tilde{\mathbf{x}}^{k-1}}{\partial \theta_{\mathcal{D}}^k} = \frac{\mathcal{D}_{cnn}^k([\mathbf{x}^0, \mathbf{x}^1, \dots, \mathbf{x}^k], \theta_{\mathcal{D}}^k)}{\partial \theta_{\mathcal{D}}^k}, \quad (6k) \\ \frac{\partial \mathbf{x}^k}{\partial \theta_{\mathcal{P}}^k} = \sum_{t=0}^{T-1} \frac{\partial \mathbf{x}_T^k}{\partial \mathbf{x}_{T-1}^k} \cdots \frac{\partial \mathbf{x}_{t+2}^k}{\partial \mathbf{x}_{t+1}^k} \cdot \frac{\partial \mathbf{x}_{t+1}^k}{\partial \beta^k} \frac{\partial \beta^k}{\partial \theta_{\mathcal{P}}^k}, \quad (6l) \\ \frac{\partial \mathbf{x}_{t+1}^k}{\partial \beta_i^k} = \theta_t^k \mathbf{F}_i^\top \mathbf{F}_i (\mathbf{x}_t^k - \mathbf{z}_i^k), \quad (6m) \\ \frac{\partial \beta^k}{\partial \theta_{\mathcal{P}}^k} = \frac{\mathcal{P}_{fcn}^k(\mathbf{d}^k, \theta_{\mathcal{P}}^k)}{\partial \theta_{\mathcal{P}}^k}. \quad (6n) \end{array} \right.$$

## II. EXPERIMENTS

### II.A. Comparison Method

#### II.A.1. MoDL

was proposed in<sup>1</sup> for MRI reconstruction. We applied it in CT. The details of unrolling stage of MoDL is as follows.

$$\begin{aligned} \mathbf{x}^k &= (\mathbf{A}^\top \mathbf{A} + \lambda \mathbf{I})^{-1} (\mathbf{A}^\top \mathbf{y} + \lambda \tilde{\mathbf{x}}^{k-1}), \\ \tilde{\mathbf{x}}^k &= \mathcal{D}_{cnn}(\mathbf{x}^k; \theta^k) \end{aligned}$$

where  $\mathcal{D}_{cnn}$  is the same neural network as AHP-Net and  $\lambda$  is set as learnable parameter. The loss of MoDL is

$$\mathcal{L}(\Theta) = \sum_{j=1}^J \|\mathbf{x}_j^K(\Theta) - \mathbf{x}_j\|_2^2.$$

where  $\Theta = (\theta^1, \dots, \theta^K, \lambda)$ . For consistency, we set  $K = 3$ . Adam optimizer was used with the momentum parameter  $\beta = 0.9$ , mini-batch size to be 4, and the learning rate to be  $10^{-4}$ . The model was trained for 50 epochs.

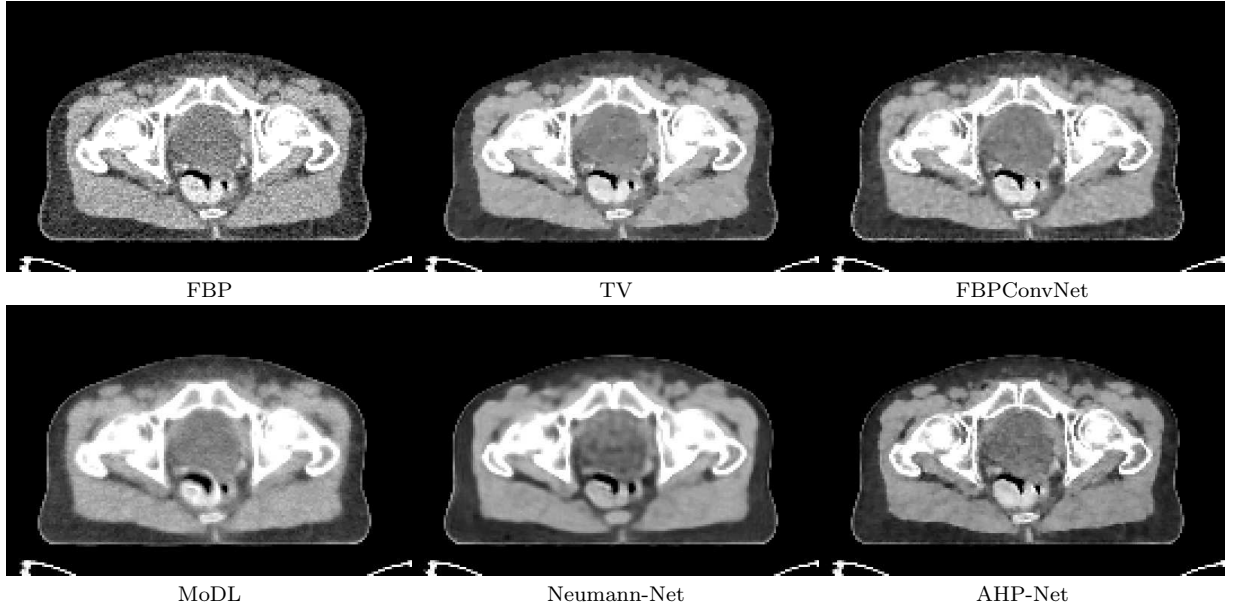


FIG. 1: Reconstruction results at dose level  $I_i = 5 \times 10^4$  by the models trained under same dose level.

### II.A.2. Neumann-Net

Neumann Network was proposed in<sup>2</sup> for linear inverse problem in imaging. With step size  $\eta > 0$ , the inverse problem can be solved by

$$\mathbf{x}^k = \eta \sum_{k=1}^K (\mathbf{I} - \eta \mathbf{A}^T \mathbf{A} - \eta \mathbf{R})^k \mathbf{A}^T \mathbf{y}.$$

The details of unrolling stage of Neumann-Net is as follows.

$$\mathbf{x}^k = \mathbf{x}^{k-1} + \eta (\mathbf{I} - \eta \mathbf{A}^T \mathbf{A}) \mathbf{x}^{k-1} - \eta \mathcal{D}_{cnn}(\mathbf{x}^{k-1}, \theta^k).$$

The loss of Neumann-Net is

$$\mathcal{L}(\Theta) = \sum_{j=1}^J \|\mathbf{x}_j^K(\Theta) - \mathbf{x}_j\|_2^2.$$

where  $\Theta = (\theta^1, \dots, \theta^K, \eta)$ . For consistency, we set  $K = 3$ . Adam optimizer was used with the momentum parameter  $\beta = 0.9$ , mini-batch size to be 4, and the learning rate to be  $10^{-4}$ . The model was trained for 50 epochs.

## III. RESULT

### III.A. Visual comparison

Fig. 1 and Fig. 3 shows the images reconstructed by the models trained under same dose level. And the corresponding zoomed-in images are displayed in Fig. 2 and Fig. 4.

Fig. 5 and Fig. 7 shows the images reconstructed by the universal models trained for varying dose levels. And the corresponding zoomed-in images are displayed in Fig. 6 and Fig. 8.

See Table I for quantitative comparison for the results shown in Fig. 1, Fig. 3, Fig. 5 and Fig. 7.

### III.B. Ablation study

Fig. 9 and Fig. 11 show the images reconstructed by different versions of the AHP-Net trained under same dose level with the dose level of  $I_i = 5 \times 10^4$  and  $I_i = 10^4$ . And their zoomed-in images are displayed in Fig. 10 and Fig. 12

<sup>1</sup>Hemant K Aggarwal, Merry P Mani, and Mathews Jacob. MoDL: Model-based deep learning architecture for inverse problems. *IEEE transactions on medical imaging*, 38(2):394–405, 2018.

<sup>2</sup>Davis Gilton, Greg Ongie, and Rebecca Willett. Neumann networks for inverse problems in imaging. *arXiv preprint arXiv:1901.03707*, 2019.

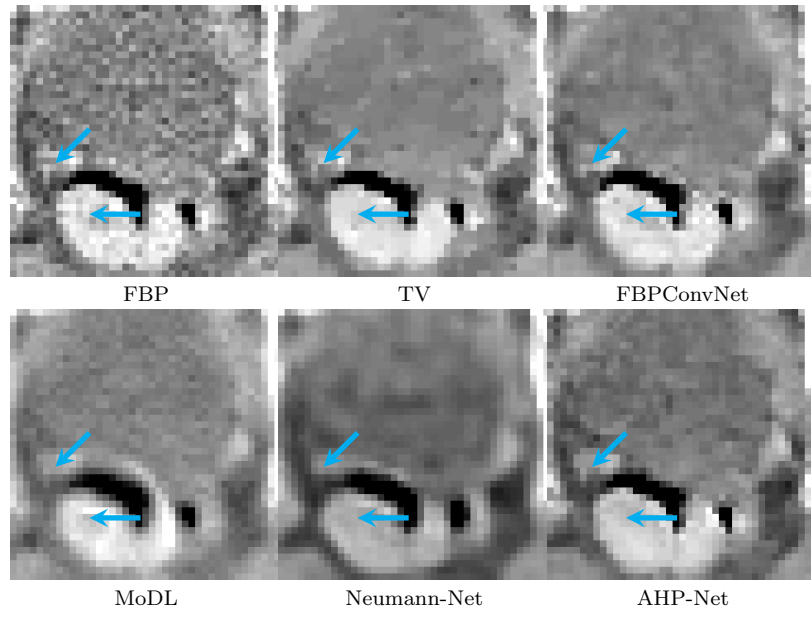
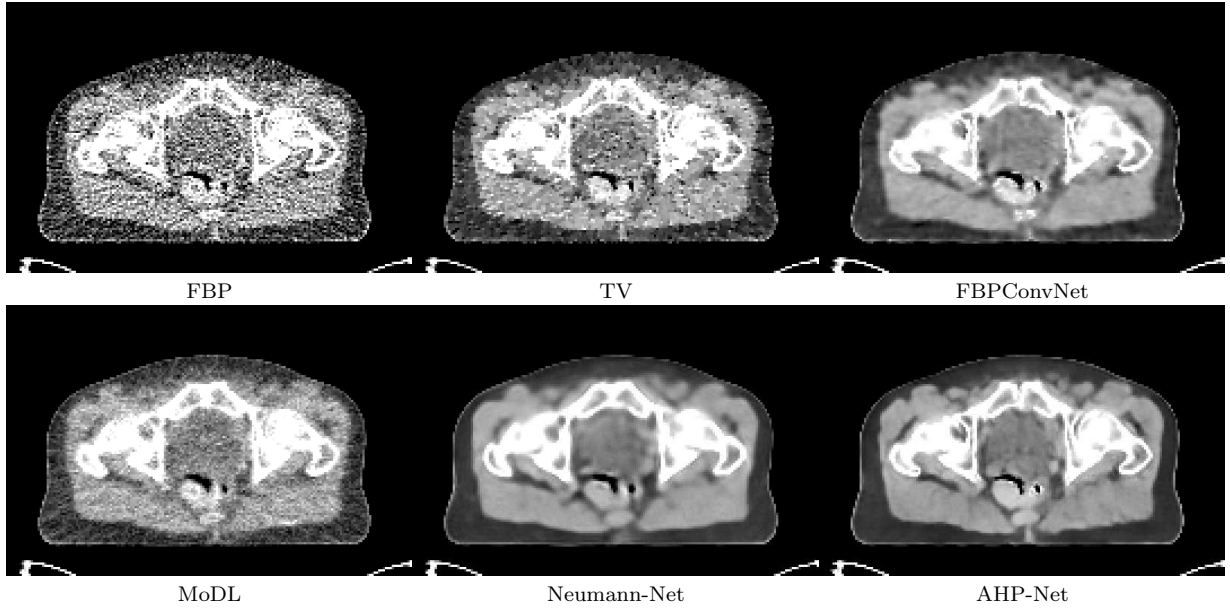


FIG. 2: Zoom-in results of Fig. 1.

FIG. 3: Reconstruction results at dose level  $I_i = 5 \times 10^3$  by the models trained under same dose level.



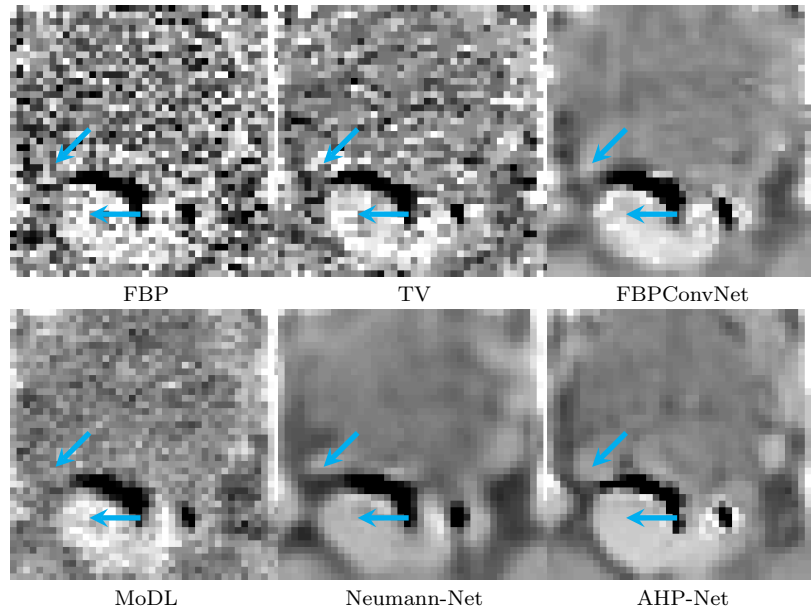
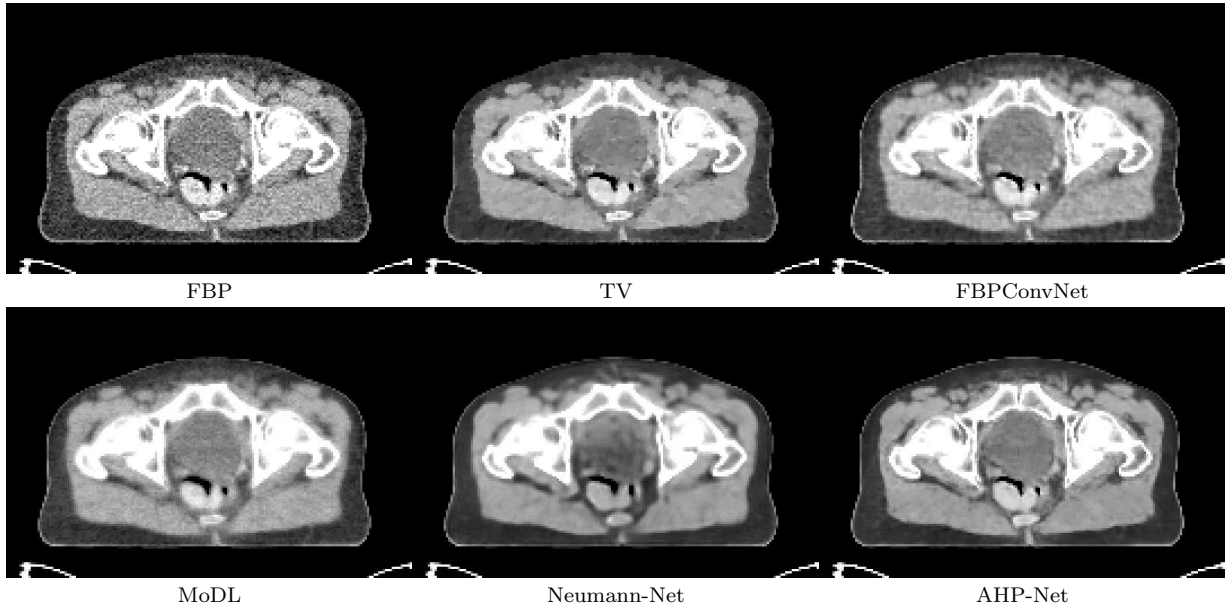


FIG. 4: Zoom-in results of Fig. 3.

FIG. 5: Reconstruction results at dose level  $I_i = 5 \times 10^4$  by the universal models trained for varying dose levels.

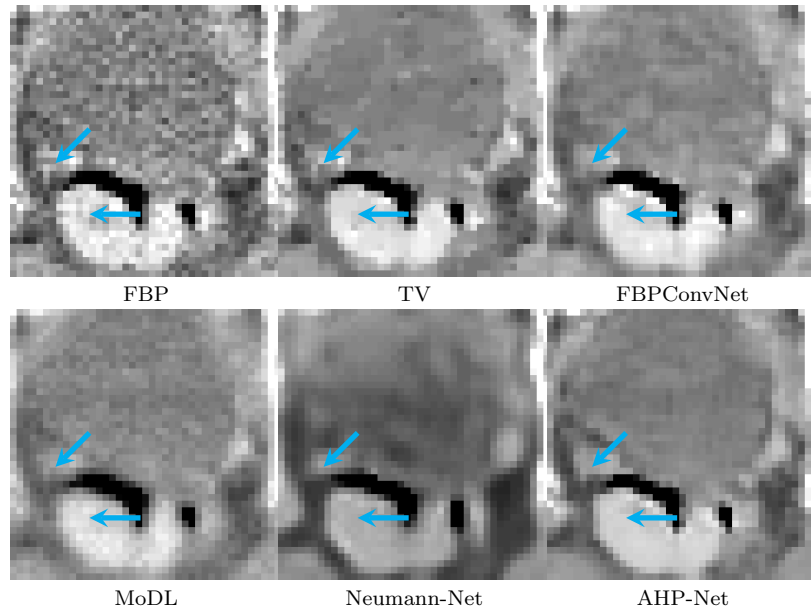
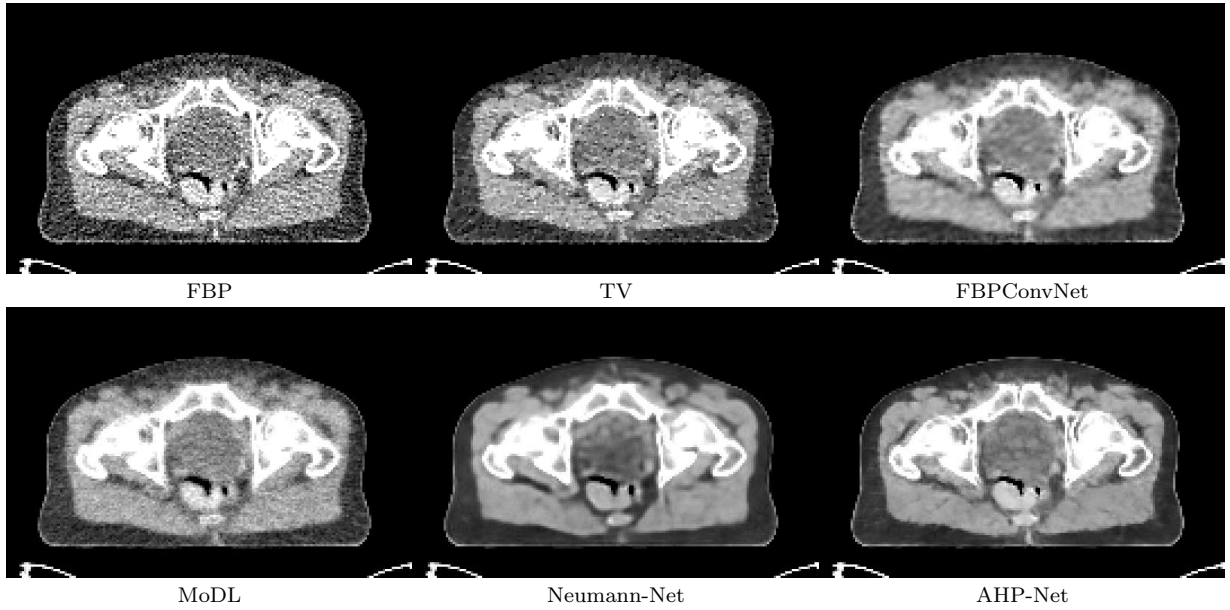


FIG. 6: Zoom-in results of Fig. 5.

FIG. 7: Reconstruction results at dose level  $I_i = 10^5$  by the universal models trained for varying dose levels.

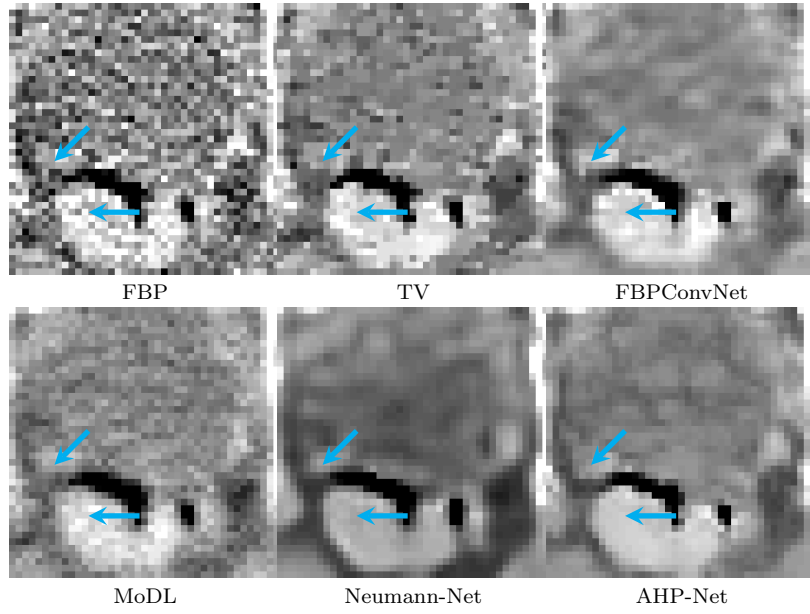


FIG. 8: Zoom-in results of Fig. 7.

TABLE I: Quantitative metrics on the reconstruction results for the image slice shown in Fig. 1, Fig. 3, Fig. 5 and Fig. 7.

Method		FBP	TV	FBPCov Net	MoDL	Neumann-Net	Our AHP-Net
Fig. 1	PSNR	38.57	41.72	42.39	37.21	36.64	43.37
	RMSE	22.08	15.37	14.22	25.81	27.58	12.70
	SSIM	0.9254	0.9716	0.9717	0.9487	0.9329	0.9789
Fig. 3	PSNR	29.05	32.62	37.70	34.39	35.48	39.30
	RMSE	66.00	43.81	24.41	35.72	31.53	20.31
	SSIM	0.5883	0.7612	0.9322	0.8327	0.9133	0.9557
Fig. 5	PSNR	38.57	41.72	41.94	37.47	37.33	42.71
	RMSE	22.08	15.37	14.98	25.05	25.46	13.71
	SSIM	0.9254	0.9716	0.9671	0.9373	0.9328	0.9748
Fig. 7	PSNR	32.70	36.69	38.34	36.17	36.83	40.09
	RMSE	43.42	27.41	22.66	29.11	26.97	18.54
	SSIM	0.7490	0.8980	0.9379	0.8781	0.9269	0.9563

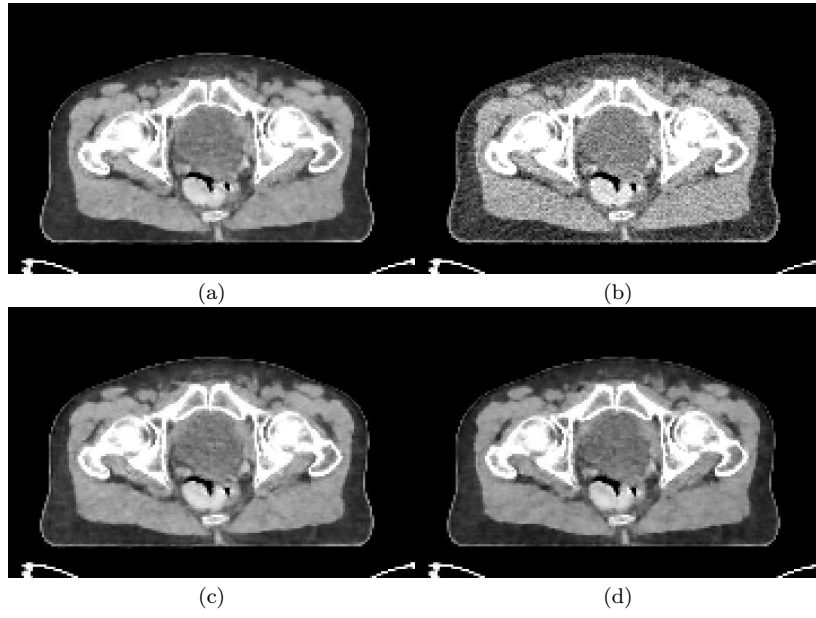


FIG. 9: Reconstruction results at dose level  $I_i = 5 \times 10^4$  by the models trained under same dose level. (a) Using  $\nabla$ ; (b) Learnable filters  $\{F_i\}$ ; (c) Learnable HP; (d) AHP-net.

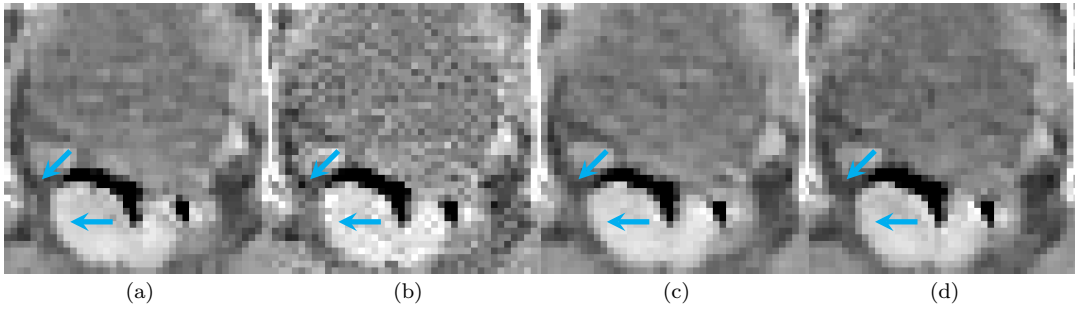


FIG. 10: Zoom-in results of Fig. 9. (a) Using  $\nabla$ ; (b) Learnable filters  $\{F_i\}$ ; (c) Learnable HP; (d) AHP-net.

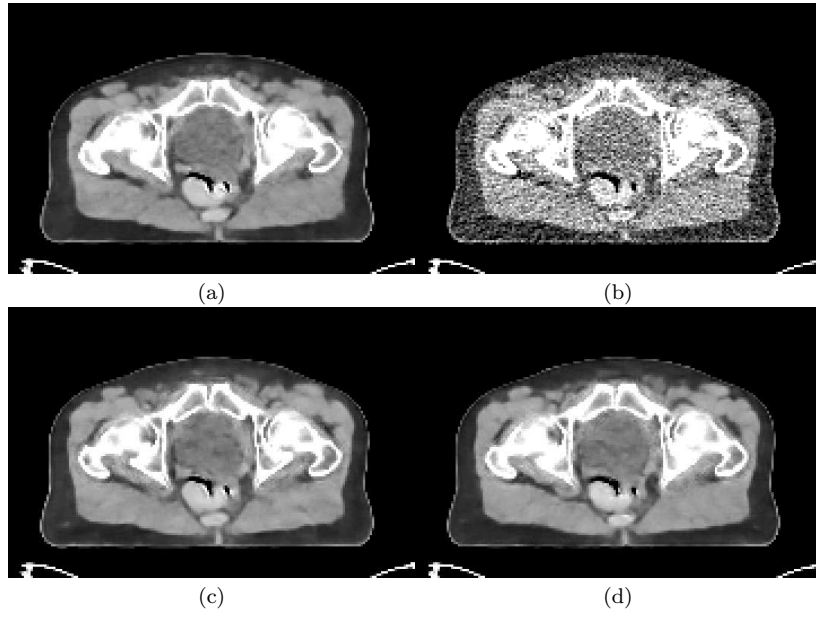


FIG. 11: Reconstruction results at dose level  $I_i = 10^4$  by the models trained under same dose level. (a) Using  $\nabla$ ; (b) Learnable filters  $\{F_i\}$ ; (c) Learnable HP; (d) AHP-net.

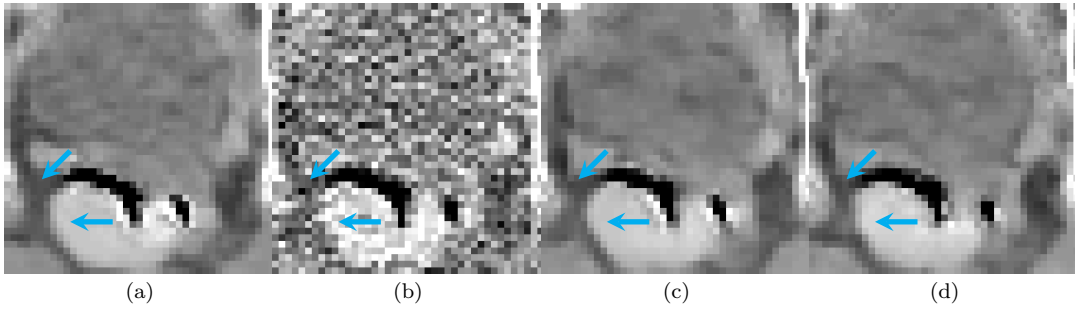


FIG. 12: Zoom-in results of Fig. 11. (a) Using  $\nabla$ ; (b) Learnable filters  $\{F_i\}$ ; (c) Learnable HP; (d) AHP-net.